

**Millimeter-Wave Backscatter Measurements in Support of Surface
Navigation Applications**

by

Brett R. J. Snuttjer

A THESIS

Presented to the Faculty of

The Graduate College at the University of Nebraska

In Partial Fulfillment of Requirements

For the Degree of Master of Science

Major: Electrical Engineering

Under the Supervision of Professor Ram M. Narayanan

Lincoln, Nebraska

December, 1996

Millimeter-Wave Backscatter Measurements in Support of Surface Navigation Applications

Brett R. J. Snuttjer, M. S.

University of Nebraska, 1996

Advisor: Ram M. Narayanan

Millimeter-wave (MMW) short range radar systems have unique advantages in surface navigation applications, such as military vehicle mobility in inclement conditions, aircraft landing assistance and missile guidance. MMW radars systems have recently become commercially affordable, and are being developed for automobile collision avoidance applications.

Two types of radar cross-section (RCS) measurements were performed at 95 GHz. Grazing angle clutter data were obtained from common surfaces. The RCS of objects, commonly encountered by automobiles on the road, was also measured. In addition, the received power statistics were investigated for both types of RCS measurements.

Surface clutter from several surfaces, including asphalt, grass and snow, was measured at 7.5° and 5.0° grazing angles. The average normalized RCS values are presented for each surface. The received clutter power is compared to Rayleigh and Weibull probability distributions. For all distributed surfaces, the received power cumulative distribution function (CDF) best matches the Rayleigh assumption.

The azimuthal RCS profile was measured and plotted for several roadside objects. These objects included both metal and wood sign posts and a section of guard rail. An average RCS value was also calculated for each object. The received power CDF was compared to the Rayleigh and Weibull distributions. The uniformly shaped targets, e.g., a round wood pole, best match the Rayleigh distribution. The majority of odd shaped objects best follow the Weibull assumption.

Acknowledgments

I gratefully acknowledge the support provided by the U.S. Air Force, Air Force Institute of Technology (AFIT) Civilian Institution program. Thanks also to Electrical Engineering department chairman, Dr. Rodney J. Soukup, for sponsoring a departmental tuition waiver. I'm looking forward to active duty service and a successful military career.

I would like to express my gratitude to Dr. Ram M. Narayanan, for his guidance and instruction during my thesis work. Thank you for your kind words of advice and contagious enthusiasm. It's been a pleasure working with you.

I also wish to thank Dr. Robert D. Palmer and Dr. Michael W. Hoffman for critically reviewing my thesis. Your technical advice and instruction are greatly appreciated.

I'm sincerely grateful to fellow ERS� Laboratory students, Praveen Hirsave and Chris Heald, for their assistance with the field measurements. I would also like to thank all my friends in ERS�, for making the work environment enjoyable and entertaining. It was an honor to work with you all.

Thanks are also due to Daniel D. Cox, MSEE-UNL 1993, who constructed the original radar system.

Finally, I want to thank my parents, Roland and Joyce, for their support and love.

Contents

Contents	i
List of Figures	iii
List of Tables	vi
1 Introduction	1
1.1 Surface Clutter	2
1.2 Roadside Object Measurements	5
2 Radar System Description	7
2.1 Radar Transmitter	7
2.2 Tx and Rx Antennas	10
2.3 Radar Receiver	10
2.4 Minimum Detectable Signal Level	15
2.5 A/D Sampling	15
3 Experiment Description	17
3.1 Far-Field Distance Considerations	17
3.2 Calibration Target	18
3.3 Surface Clutter Measurements	18
3.4 Roadside Object RCS Measurements	22
4 Data Analysis	25
4.1 Surface Clutter Normalized RCS	25

4.2	Roadside Object RCS	28
4.3	Radar Range Equation Parameters	29
4.4	Rayleigh Distribution Comparison	29
4.5	Weibull Distribution Comparison	32
5	Surface Clutter Measurements	35
5.1	Asphalt Parking Lot	35
5.2	Gravel Parking Lot	39
5.3	Dry Snow Results	44
5.4	Dry Soil Results	47
5.5	Grass Surface Results	50
6	Roadside Object Measurements	55
6.1	Round Pole, Wood	56
6.2	Square Pole, Wood	61
6.3	I-Beam Post, Metal	65
6.4	Utility Post, Metal	69
6.5	Small U-Channel, Metal	73
6.6	Large U-Channel, Metal	77
6.7	Guard Rail Measurements	81
7	Conclusions	85
	Appendices	89
A	89
B	93
C	100
	Bibliography	108

List of Figures

1.1	Rayleigh Scattering Model	4
2.1	95 GHz Radar System Block Diagram	8
2.2	Log-Amplifier Calibration	13
3.1	Surface Clutter Experiment Setup	19
3.2	Radar Scan Diagram	21
3.3	RCS Measurement-Experiment Setup	23
5.1	Asphalt CDF, at 7.5° and 5.0°	38
5.2	Dry Gravel CDF, at 7.5° and 5.0°	42
5.3	Wet Gravel CDF, at 7.5° and 5.0°	43
5.4	Dry Snow CDF, at 7.5° and 5.0°	46
5.5	Dry Soil CDF, at 7.5° and 5.0°	49
5.6	Short Grass CDF, at 7.5° and 5.0°	53
5.7	Tall Grass CDF, at 7.5° and 5.0°	54
6.1	Round Wood RCS (dBsm) at 12m (a) VV Pol. (b) HH Pol.	58
6.2	Round Wood Pole CDF, 12m	60
6.3	Square Wood Pole RCS (dBsm) at 12m (a) VV Pol. (b) HH Pol.	62
6.4	Square Wood Pole CDF, 12m	64

6.5	I-Beam RCS (dBsm) at 12m (a) VV Pol. (b) HH Pol.	66
6.6	I-Beam CDF, 12m	68
6.7	Utility Post RCS (dBsm) at 12m (a) VV Pol. (b) HH Pol.	70
6.8	Utility Post CDF, 12m	72
6.9	Small U-Channel RCS(dBsm) at 12m (a) VV Pol. (b) HH Pol.	74
6.10	Small U-Channel CDF, 12m	76
6.11	Large U-Channel RCS(dBsm) at 12m (a) VV Pol. (b) HH Pol.	78
6.12	Large U-Channel CDF, 12m	80
6.13	Guard Rail RCS(dBsm) at 15m (a) VV Pol. (b) HH Pol.	82
6.14	Guard Rail CDF, 15m	84
A.1	MMW Radar Transmitter	90
A.2	Dielectric Horn Antenna	90
A.3	MMW Radar Receiver	91
A.4	HP-8620C Sweep Oscillator	91
A.5	2nd IF Stage	92
A.6	Tetrahedral Corner Reflector	92
B.1	Asphalt Surface	94
B.2	Dry Gravel Surface	95
B.3	Dry Snow Surface	96
B.4	Dry Soil Surface	97
B.5	Short Grass Surface	98
B.6	Tall Grass Surface	99
C.1	Top, Round Wood Pole	101
C.2	Round Wood Pole	101

C.3 Top, Square Wood Pole	102
C.4 Square Wood Pole	102
C.5 Top, I-Beam Post	103
C.6 I-Beam Post	103
C.7 Top, Utility Post	104
C.8 Utility Post	104
C.9 Top, Small U-Channel Post	105
C.10 Small U-Channel Post	105
C.11 Top, Large U-Channel Post	106
C.12 Large U-Channel Post	106
C.13 Top, Guard Rail Section	107
C.14 Guard Rail Section	107

List of Tables

2.1	Gunn Oscillator and Modulator/Regulator Specifications	9
2.2	W-Band Isolator Specifications	9
2.3	Antenna Specifications	10
2.4	85 GHz Local Oscillator Specifications	11
2.5	W-Band Mixer Specifications	11
2.6	X-Band Amplifier Specifications	12
2.7	X-Band Mixer Specifications	13
2.8	HP-8620C and HP-86290A Specifications	14
2.9	60 MHz Amplifier Specifications	14
2.10	Log. Amplifier Specifications	15
3.1	Surface Clutter Measurement Sample Parameters	22
4.1	Radar Range Equation Parameters	30
4.2	Surface Clutter Parameters, at 7.5° and 5.0°	30
5.1	Asphalt Sigma-zero Results	36
5.2	Asphalt Received Power Statistics	37
5.3	Dry Gravel Sigma-zero Results	40
5.4	Wet Gravel Sigma-zero Results	40
5.5	Dry Gravel Received Power Statistics	41

5.6	Wet Gravel Received Power Statistics	41
5.7	Dry Snow Sigma-zero Results	45
5.8	Clutter Model, VV or HH Sigma-zero Results	45
5.9	Dry Snow Received Power Statistics	46
5.10	Dry Soil Sigma-zero Results	47
5.11	Dry Soil Received Power Statistics	48
5.12	Short Grass Sigma-zero Results	51
5.13	Tall Grass Sigma-zero Results	51
5.14	Short Grass Received Power Statistics	52
5.15	Tall Grass Received Power Statistics	52
6.1	Round Wood Pole RCS Results	57
6.2	Round Pole, Received Power Statistics, 12m	59
6.3	Round Pole, Received Power Statistics, 16m	59
6.4	Square Wood Pole RCS Results	61
6.5	Square Pole Power Statistics, 12m	63
6.6	Square Pole Power Statistics, 16m	63
6.7	I-Beam RCS Results	65
6.8	I-Beam Received Power Statistics, 12m	67
6.9	I-Beam Received Power Statistics, 16m	67
6.10	Utility Post RCS Results	69
6.11	Utility Post Received Power Statistics, 12m	71
6.12	Utility Post Received Power Statistics, 16m	71
6.13	Small U-Channel RCS Results	73
6.14	Small U-Channel Received Power Statistics, 12m	75
6.15	Small U-Channel Received Power Statistics, 16m	75

6.16 Large U-Channel RCS Results	77
6.17 Large U-Channel Received Power Statistics, 12m	79
6.18 Large U-Channel Received Power Statistics, 16m	79
6.19 Guard Rail RCS Results	81
6.20 Guard Rail Received Power Statistics, 15m	83
6.21 Guard Rail Received Power Statistics, 20m	83
B.1 Asphalt Surface Ground Truth	94
B.2 Gravel Surface Ground Truth	95
B.3 Dry Snow Ground Truth	96
B.4 Dry Soil Ground Truth	97
B.5 Short Grass Ground Truth	98
B.6 Tall Grass Ground Truth	99

Chapter 1

Introduction

The development of millimeter-wave (MMW) radar systems has advanced rapidly in the last six years. Fabrication of new monolithic microwave integrated circuits (MMIC) chips have made high-frequency radars and radiometers more affordable for both military and commercial applications. A high-frequency MMIC chip integrates a radar transmitter and receiver on a microstrip circuit. MMIC fabrication also minimizes the radar system size. Several U.S. companies, including Avantek, Lockheed-Martin and TRW, are developing W-Band MMIC chips at 94 GHz [1]. W-Band operating frequencies near 94 GHz are desired, because the atmospheric attenuation is minimized in this frequency window.

Several military and commercial applications exist for MMW radar systems. Missile guidance, aircraft landing assistance and automobile collision avoidance are three examples [2]. MMW radar systems provide acceptable angular resolutions, but are superior to optical systems in conditions of rain, fog, or smoke.

The University of Nebraska-Lincoln (UNL) has developed a continuous-wave (CW) 95 GHz MMW radar system. The radar is capable of measuring radar cross sections for VV, HH and VH polarization combinations in both monostatic and bistatic con-

figurations. The measurements described in this thesis were performed in a quasi-monostatic configuration. The radar system is discussed further in Chapter 2. Two different experiments, normalized surface clutter radar cross-section (RCS) and roadside object RCS measurements, were performed at 95 GHz. The experiment setup, for both measurement types, are discussed in Chapter 3. The equations used in the measurements, including the monostatic radar range equation, are presented in Chapter 4. The received power probability statistics are also considered. A received power cumulative distribution function (CDF) is obtained from the sampled data. The experimental CDF is compared to Rayleigh and Weibull CDF's. Results for surface clutter RCS and roadside object RCS measurements are presented in Chapters 5 and 6.

1.1 Surface Clutter

Surface clutter measurements, at grazing angles of 7.5° and 5.0° , were performed for several surfaces. "Grazing angle" is defined as the angle between the mean surface and the incident wave. The grazing angle is the complement of the incident angle. Sigma-zero values at VV, HH and VH polarizations were measured. Sigma-zero is a normalized parameter, defined as RCS per unit area. The surfaces include asphalt, grass, gravel, snow and soil. Attempts were made to characterize the sigma-zero variability, due to differing environmental conditions. Sigma-zero variations are primarily caused by changes in moisture level and surface roughness. Wet and dry gravel measurements were obtained, as well as short and tall grass measurements. The experimental data are expected to aid in the development of MMW missile guidance and aircraft landing systems.

Extensive W-Band (95 GHz) clutter measurements have been performed by the Georgia Institute of Technology. Average sigma-zero values were obtained for grazing

angles between 70° to 10° . The focus of the study was on characterizing surface clutter from trees, grass, and both wet and refrozen snow. Georgia Tech researchers developed a clutter model, for all four surfaces, from the experimental data. The model was extended to grazing angles lower than 10° by extrapolating the measured average sigma-zero values. The clutter model is given in Equation 1.1, where A, B and C are the experimentally derived parameters, and Θ_g in radians, is the grazing angle [3]:

$$\sigma^\circ = A (\Theta_g + C)^B \quad (1.1)$$

It is important to compare the clutter model to experimental data below 10° grazing, to determine the validity of the model. Experimental results from both grass and snow surfaces are compared to the clutter model in Chapter 5.

Grazing angle surface clutter measurements, for asphalt and rough ground, were recently presented at the 1996 IEEE National Radar Conference [4]. Our experimental results are compared to the published measurements in Chapter 5.

It is important to define radar clutter and discuss the parameters related to clutter, including radar frequency and angle of incidence. Radar clutter is defined as unwanted signal return from various sources that interfere with target detection. The sources of clutter can be classified as two types, atmospheric and surface clutter. Sources of atmospheric clutter include rain, fog and clouds. Some examples of surface clutter are trees, buildings, snow, asphalt and grass surfaces.

The amplitude distribution and spectral characteristics of clutter are both important in radar measurements. The focus of the thesis is on the surface clutter amplitude properties. The clutter amplitude distribution is important when determining desired target-to-clutter ratios and maintaining a constant false alarm rate

(CFAR). A CFAR is important in threshold detection type radars. Clutter amplitude is typically measured as a normalized parameter. The clutter sigma-zero, or σ^0 , normalized value is defined as the RCS per unit area.

Radar scattering from a surface depends primarily on the surface roughness. The Rayleigh scattering model [5] is commonly used to classify the surface “smooth” or “rough”. The Rayleigh roughness criteria depends on the incident wavelength λ , the grazing angle Θ_g , and the surface roughness Δh . The Rayleigh scattering model is shown in Figure 1.1. Using the Rayleigh model, a surface is smooth if Equation 1.2 is satisfied:

$$\Delta h \sin\Theta_g < \frac{\lambda}{8} \quad (1.2)$$

Rayleigh Scattering Criteria

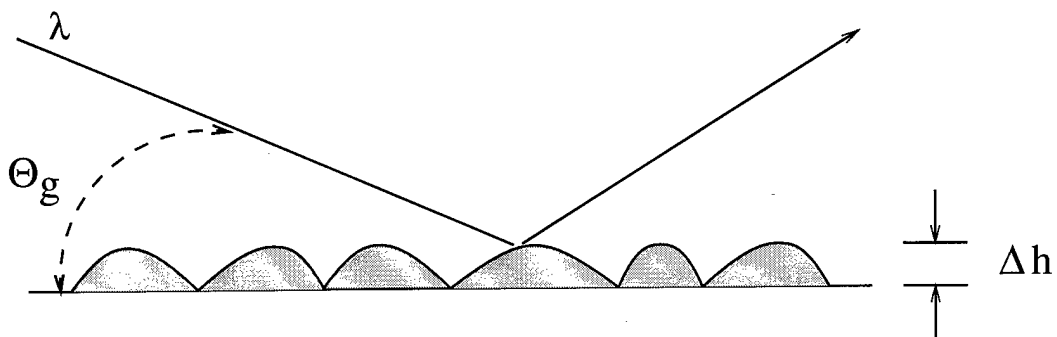


Figure 1.1: Rayleigh Scattering Model

The radar signal reflected from a surface has two components, the specular and the diffuse component [5]. The reflected specular component has a deterministic phase relationship to the incident wave. The diffuse component has a random phase

relationship. The specular and diffuse components are also referred to as coherent and non-coherent components, respectively. The specular and diffuse scattering components are important when considering both co-polarization and cross-polarization measurements. Scattering from a “smooth” surface, such as an asphalt parking lot, is mostly specular. The cross-pol scattering from a “smooth” surface is minimal. Both co-pol and cross-pol surface clutter measurements were performed.

The surface clutter normalized RCS, or sigma-zero, is a complex parameter that depends on incident angle, wavelength and the surface parameters. Therefore, the surface scattering at W-Band frequencies is a non-linear phenomenon. It is obviously not possible to scale existing X-Band sigma-zero measurements up to W-Band frequencies. The only practical way to characterize MMW surface clutter is by experimental measurements.

1.2 Roadside Object Measurements

The international automobile industry has indicated a need for new collision avoidance and automated cruise control technologies. Automobile collision avoidance/obstacle detection systems have been in development since the late 1980's. One automobile industry study indicated that 60% of rear-end collisions could be avoided if drivers had an extra 0.5 seconds to react [6]. The first systems operated in the Ka-Band (27 to 40 GHz), but better accuracy was required in the high clutter roadway situation. Millimeter-wavelength radar provides better angular resolution and smaller antenna size requirements.

The development of W-Band MMIC's has made high frequency MMW collision avoidance systems a reality. The European automobile industry has allocated the 76 to 77 GHz band for anti-collision radar systems [7]. A 77 GHz automated cruise

control system is currently being developed in Sweden [8]. The system has been successfully tested in controlled conditions and in actual highway settings. No information on U.S. developed automobile radar systems was available.

Radar cross-section (RCS) measurements of several roadside objects were performed at 95 GHz. These RCS measurements are expected to support the development of U.S. collision avoidance radar systems. Several types of sign posts were measured, including both wood and metal sign posts. A guard rail section was also measured. All of the objects measured are common obstacles encountered when driving. A profile of RCS versus aspect angle is presented in Chapter 5.

There is little known about the RCS of roadside objects at 95 GHz. Radar cross-section measurements of two typical vehicles were recently presented by Yamaguchi [4]. There have been no published RCS results, at any frequency, for sign posts or other common roadside objects.

Chapter 2

Radar System Description

The MMW radar system used in our measurements operates in continuous wave (CW) mode. A block diagram of the radar system is shown in Figure 2.1. The transmit frequency is 95 GHz. The frequency source used is a solid-state Gunn Oscillator. A two stage superheterodyne receiver configuration down converts the received signal to 60 MHz. A 60 MHz logarithmic amplifier converts the received signal power to a voltage level. This voltage level is sampled by a PC controlled A/D board.

The following chapter discusses the system in more detail, including the transmitter, receiver, both Tx and Rx antennas, and the PC controlled voltage sampling. Overall system noise figure and minimum signal-to-noise ratio (SNR) are also discussed. The original radar system was constructed by Daniel Cox in 1992. Several system modifications were made for my experimental measurements. The receiver control and biasing circuitry was redone and the logarithmic amplifier was added to the receiver.

2.1 Radar Transmitter

A Gunn Oscillator from Millitech is used as the frequency source. The output power is 40 mW at 95 GHz. The Gunn Oscillator is an Indium-Phosphide solid state source,

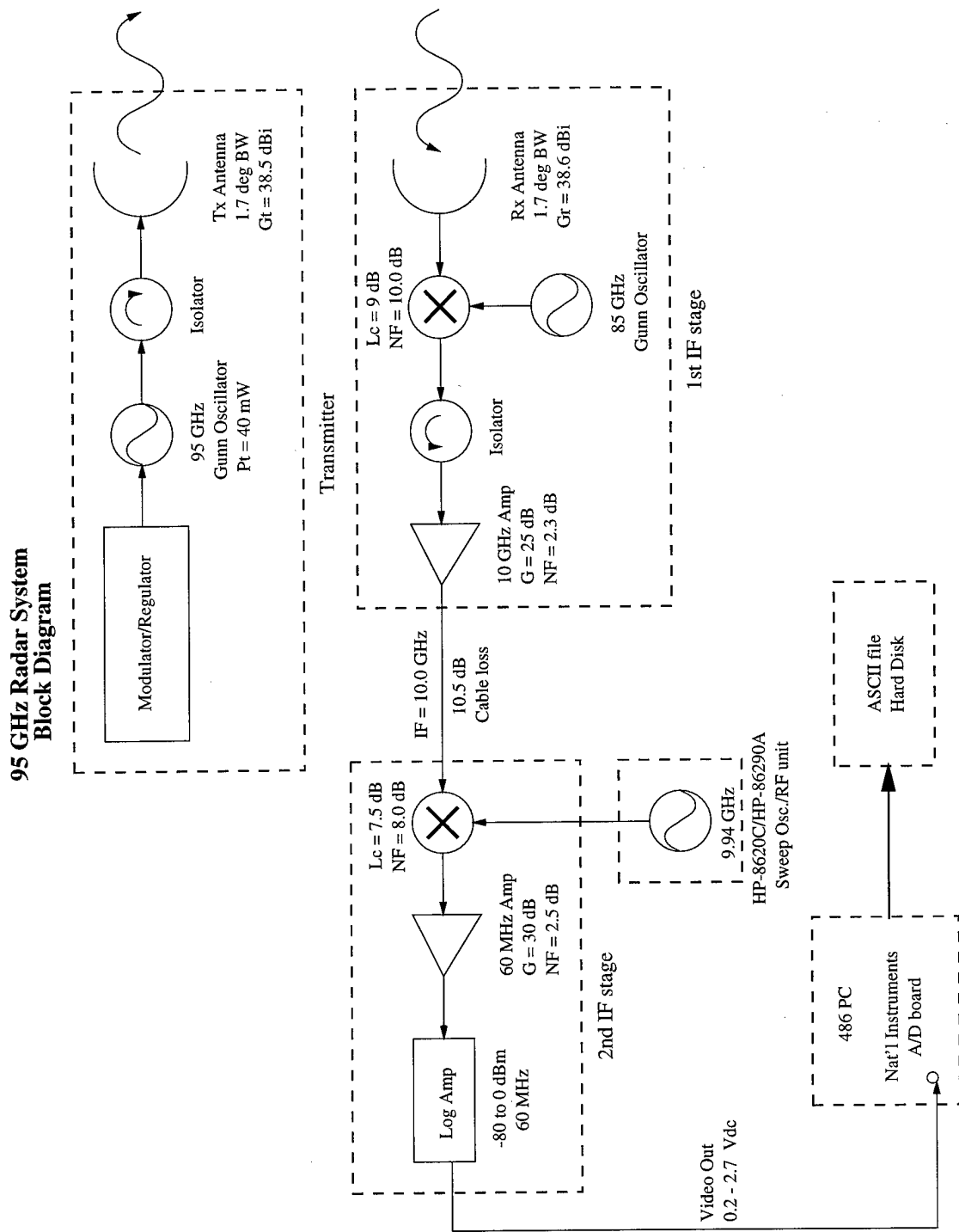


Figure 2.1: 95 GHz Radar System Block Diagram

which is voltage biased by a modulator/regulator control unit. The Gunn Oscillator is operated in CW mode, but could be frequency modulated by the Modulator/Regulator unit. Table 2.1 lists the Gunn Oscillator and Modulator/Regulator unit specifications.

Table 2.1: Gunn Oscillator and Modulator/Regulator Specifications

Manufacturer	Millitech
Operating Freq.	95 GHz
Freq. Modulation	± 100 kHz (max)
Power Out	+40 dBm
Voltage bias	+9.88 Vdc (@95 GHz)
Current	132 mA

A W-Band Isolator is connected between the Gunn Oscillator and the Tx antenna. The Isolator provides a better impedance match, thus lowering the Voltage Standing Wave Ratio (VSWR). Table 2.2 shows the W-band Isolator specifications. The Gunn

Table 2.2: W-Band Isolator Specifications

Manufacturer	Millitech
Center Freq.	95 GHz
Bandwidth	± 500 MHz
Insertion Loss	≤ 0.8 dB
Isolation	≥ 20 dB

Oscillator, Isolator and Tx antenna are housed in a separate enclosure, shown in Appendix A, Figure A.1.

2.2 Tx and Rx Antennas

Two separate dielectric horn antennas are used in the radar system. The Tx and Rx antennas are identical, except for a slight difference in antenna gain. A dielectric horn antenna has high gain, low beamwidth, a Gaussian beam shape and low sidelobes. Appendix A, Figure A.2 is a photo of the transmit antenna. The meniscus shaped dielectric lens performs phase correction on the input signal energy. The resulting radiated signal is a phase-collimated plane wave. Table 2.3 lists the Tx and Rx antenna specifications.

Table 2.3: Antenna Specifications

Manufacturer	Millitech
Operating Freq.	95 GHz
Beamwidth	1.7°
Sidelobes	≤ -18.0 dBi
Lens diameter	5.0 in.
Gain-Tx	38.5 dBi
Gain-Rx	38.6 dBi

2.3 Radar Receiver

The radar receiver consists of the Rx antenna and two Intermediate-Frequency (IF) stages. This configuration is typically referred to as a superheterodyne receiver. The receiver bandwidth is 10 MHz. The overall gain of the receiver is approximately 37.5 dB.

The first IF stage and the Rx antenna are housed in an enclosure similar to the transmitter enclosure. Figure A.3 is a photo of the first IF stage enclosure. In the first IF stage, the received 95 GHz signal is mixed with an 85 GHz local oscillator source. An X-band isolator is connected at the output of the mixer. The down converted 10 GHz signal is amplified and connected to the second IF stage by a 4 meter long cable. The cable attenuation is approximately 10.5 dB at 10 GHz. The first IF stage component specifications are listed in Tables 2.4 to Table 2.6:

Table 2.4: 85 GHz Local Oscillator Specifications

Manufacturer	Millitech
Operating Freq.	85 GHz
Power Out	+26 dBm (@85 GHz)
Voltage Bias	9.94 Vdc (@85 GHz)
Current	203 mA

Table 2.5: W-Band Mixer Specifications

Manufacturer	Millitech
RF Freq.	95.0 ± 0.7 GHz
IF Bandwidth	10.0 ± 0.7 GHz
LO Power Min.	+10 dBm
Noise Figure	8.0 dB max.
Conv. Loss	9.0 dB max.

Table 2.6: X-Band Amplifier Specifications

Manufacturer	Miteq
RF Freq.	8.0 - 12.0 GHz
Noise Figure	2.3 dB (@10.0 GHz)
Gain	+25.0 dB (@10.0 GHz)
Pout (1dB comp.)	+10 dBm
Voltage Bias	+15 Vdc
Current	98 mA

In the second IF stage, a 9.94 GHz LO source is mixed with the 10 GHz signal. The 9.94 GHz source used is a HP-8620C sweep oscillator with a HP-86290A RF plug-in unit. Figure A.4 shows the HP sweep oscillator and plug-in unit. The resulting 60 MHz IF frequency is amplified and connected to a logarithmic amplifier. The receiver bandwidth is limited to 10 MHz by the 60 MHz amplifier. The amplifier converts the received signal power to a voltage value. The input power to output voltage conversion is estimated from a calibration curve. The calibration curve is generated by measuring the output at different input power levels. The log amp dynamic range is -80 to 0 dBm. Figure 2.2 is a plot of the logarithmic amplifier calibration.

Figure A.5 is a photo of the second IF stage enclosure, the second IF mixer, 60 MHz amplifier and log amplifier. Table 2.7 thru Table 2.10 list the second IF stage component specifications:

Log-Amplifier Calibration

15 June, 1996

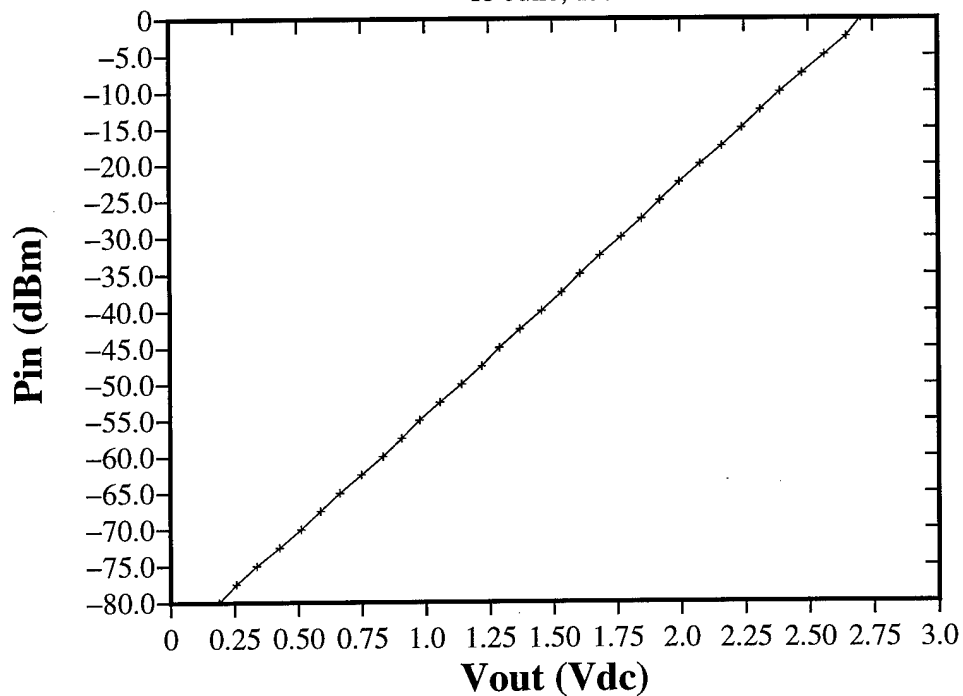


Figure 2.2: Log-Amplifier Calibration

Table 2.7: X-Band Mixer Specifications

Manufacturer	Millitech
RF Freq.	8.0 - 12.0 GHz
IF Bandwidth	DC to 400 MHz
LO Power Min.	+8 dBm
Noise Figure	8.0 dB max.
Conv. Loss	7.5 dB max.

Table 2.8: HP-8620C and HP-86290A Specifications

Manufacturer	Hewlett-Packard
RF Freq.	6.0 - 12.4 GHz
Vernier Accuracy	± 2 MHz
Freq. Stability	± 1 MHz/ $^{\circ}$ C
Power Out	$\geq +5$ dBm

Table 2.9: 60 MHz Amplifier Specifications

Manufacturer	Radar Tech. Inc.
IF Freq.	60 MHz
Bandwidth	10 MHz
Noise Figure	2.5 dB max.
Gain	+30.0 dB
Pout (1dB comp.)	+10 dBm
Voltage Bias	+15 Vdc
Current	125 mA

Table 2.10: Log. Amplifier Specifications

Manufacturer	Radar Tech. Inc.
IF Freq.	60 MHz
Bandwidth	20 MHz
Dynamic Range	-80 to 0 dBm
Sensitivity	25mV/dBm
Linearity	± 1.0 dB
Voltage Bias	± 15 Vdc
Current	177 mA

2.4 Minimum Detectable Signal Level

The overall receiver noise power, P_n , is needed to calculate the radar system minimum detectable signal (MDS) level [9]:

$$P_n = k T B F \quad (2.1)$$

Where T is room temperature (300° K), and k is Boltzman's constant. B is the radar system bandwidth, previously given to be 10 MHz. The parameter F is the radar receiver noise figure. The overall receiver noise figure is calculated to be $F = 12.3$ dB [10]. The resulting P_n is -91.5 dBm. Adding the overall receiver gain to the receiver noise power yields the minimum SNR of the radar system. Therefore, the minimum detectable signal level is approximately -54.0 dBm.

2.5 A/D Sampling

A National Instruments A/D board is used to sample the logarithmic amplifier output voltage. The A/D board is installed in a 486 personal computer. A data-acquisition

program, written in C++, controlled the sample rate and scan time of the A/D board. Chapter 4 discusses in more detail the sample rate(s) and scan time(s) used in the experiments. Each voltage value is represented by a 16 bit integer. The sampled voltage values were then converted and stored in ASCII format. Each ASCII voltage value is accurate to the sixth significant digit.

Chapter 3

Experiment Description

The following chapter describes the experiment set-up for both surface clutter and roadside object cross-section measurements. Block diagrams for both measurement types are included. Also discussed are the far-field distance consideration and the calibration target used in the experiments. The method of radar system calibration and antenna alignment is also covered. Uncorrelated sampling considerations, including the sample rate and scan time used, will also be discussed.

3.1 Far-Field Distance Considerations

The far-field distance is the minimum required distance from the radar system to the target. The minimum distance restriction ensures that the incident wave on the target is a plane wave. Equation 3.1 is the far-field distance equation[11]:

$$R_{ff} = \frac{2 D^2}{\lambda} \quad (3.1)$$

With antenna diameter $D = 12.7$ cm, and $\lambda = 3.1579$ mm at 95 GHz, the far-field distance is $R_{ff} = 10.215$ m.

3.2 Calibration Target

A tetrahedral corner, with side length $l = 13.97$ cm (5 1/2 in.), was used as the calibration target during the experimental measurements. Figure A.6, in Appendix A, is a photo of the constructed corner reflector. The radar cross-section of the corner reflector is calculated from the following equation [12]:

$$\sigma = \frac{4 \pi l^4}{3 \lambda^2} \quad (3.2)$$

At 95 GHz, the cross-section of the corner reflector is $\sigma = 159.985$ m² (+ 22.04 dBsm).

The corner reflector was used to align both antennas and to calibrate the overall radar system gain. Precise antenna alignment is important because the antenna beamwidth is small. If the antennas are misaligned, the Tx and Rx beamwidths will not overlap. Antenna alignment was ensured by placing the calibration target at the same distance as the experimental target. The transmitter and receiver enclosures were then aligned, to maximize the received power. The received voltage value was recorded, in order to calibrate the radar system gain. The calibration target was then removed and the radar system was scanned over the surface.

3.3 Surface Clutter Measurements

The experiment setup for the surface clutter measurements is shown in Figure 3.1. The Tx and Rx enclosures are both mounted on a 1.2 m diameter turntable. The resulting height of the radar system above the ground, is $h = 1.57$ m. The turntable was spatially scanned over the surface at a constant depression angle, Θ_d . The maximum depression angle, $\Theta_{dmax} = 8.84^\circ$, is set by the far-field distance. The minimum depression angle was limited by the transmitted power, $P_t = 40$ mW, and the radar system noise power, $P_n = -91.5$ dBm. Below $\Theta_{dmin} \approx 4.0^\circ$, the received clutter power

MMW Clutter Measurement Experiment Setup

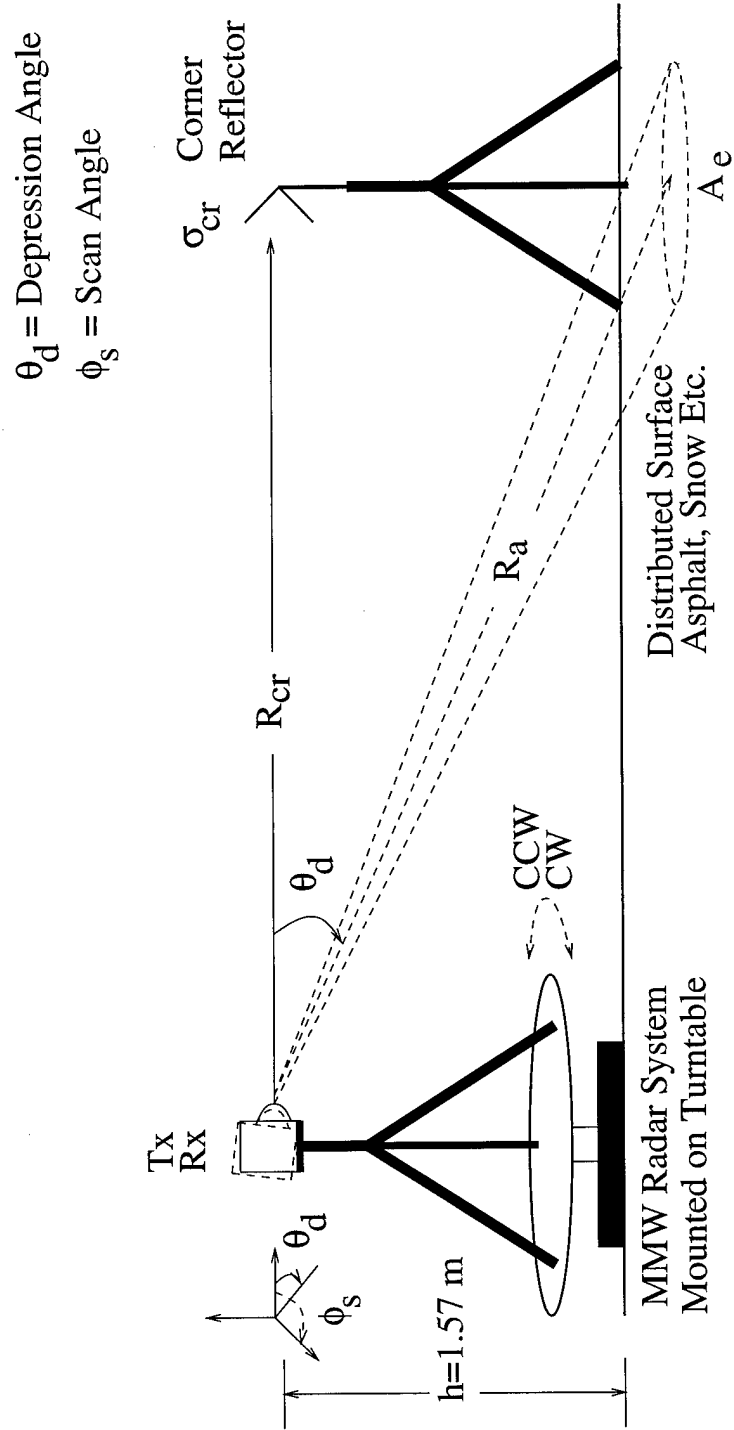


Figure 3.1: Surface Clutter Experiment Setup

is not above the radar system minimum detectable signal level. Therefore, the surface clutter measurements performed at two angles, 7.5° and 5.0° . The received voltage from the log amplifier was sampled and stored during both clockwise and counter-clockwise scans. A minimum of six scans, three each direction, were performed for each depression angle and polarization. The surface clutter was measured at HH, VV and VH polarizations.

The issue of uncorrelated sampling is important, when determining the desired experimental sample rate. A sampling guideline, to ensure sample-to-sample independence, is suggested by Ulaby et al. [13]. The guideline suggests that, for uncorrelated samples, the illuminated area must move $1/2$ a beamwidth between samples. The uncorrelated sampling guideline can be determined from the surface clutter experiment setup. During the radar system rotation, the number of independent samples depends on the total distance scanned and $1/2$ of the azimuthal beamwidth. Equation 3.3 is the distance S , traveled by the beam, during the radar scan:

$$S = R_a \phi_s \quad (3.3)$$

The distance to the surface, R_a is given by the Equation 3.4:

$$R_a = \frac{h}{\sin \Theta_d} \quad (3.4)$$

The azimuthal beamwidth W also depends on R_a , and the antenna beamwidth, $\Theta_{BW} = 1.7^\circ$ (0.0297 rad). W is defined by Equation 3.5:

$$W = R_a \Theta_{BW} \quad (3.5)$$

Figure 3.2 is a diagram of the radar scan geometry. The degree of scan, ϕ_s , was 90°

Radar Scan Diagram Surface Clutter Measurements

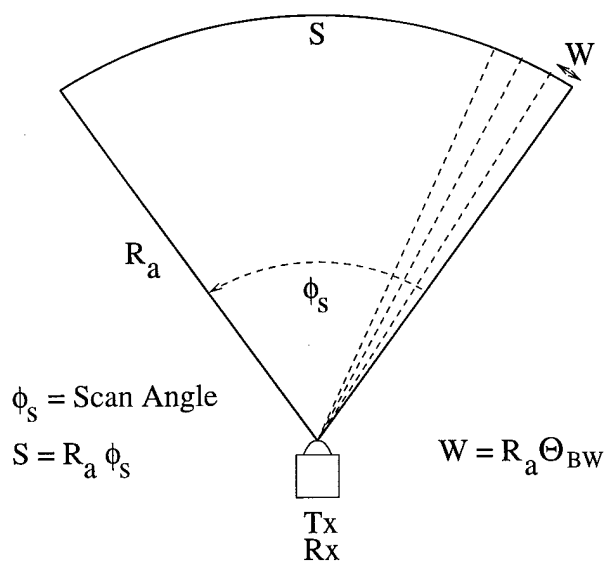


Figure 3.2: Radar Scan Diagram

during the experimental measurements. The number of uncorrelated samples N_{un} , is given by Equation 3.6:

$$N_{un} = \frac{S}{(W/2)} \quad \text{samples} \quad (3.6)$$

The suggested number is $N_{un} = 106$, for both 7.5° and 5.0° grazing angles.

The independent sampling guideline is a conservative estimate. The actual sample rate chosen was four times the suggested value. The actual number of samples measured is therefore $N_{act} = 425$ samples. The required sample rate SR , for N_{act} samples, was then determined from the turntable scan rate ω (rad/sec), the number of samples taken N_{act} , and the degree of scan ϕ_s . The desired sample rate, $SR = 70.81$ samp/sec, is found from Equation 3.7:

$$SR = \frac{N_{act} \omega}{\phi_s} \quad \text{samp/sec} \quad (3.7)$$

Table 3.1 lists the important sampling parameters, with $\phi_s = 1.5708$ radians (90°), and $\omega = 0.2617$ rad/sec.

Table 3.1: Surface Clutter Measurement Sample Parameters

Θ_d	R_a (m)	S (m)	W/2 (m)	N_{un} (samp)	N_{act} (samp)
7.5°	12.03	18.90	0.1785	106	425
5.0°	18.01	28.29	0.2672	106	425

Calibration was performed by setting the corner reflector at distance R_{cr} , equal to the distance R_a , for both depression angles. At $\Theta_d = 7.5^\circ$, for example, the corner reflector was placed at $R_{cr} = R_a = 12.03$ m. This ensured that the Tx and Rx antennas were properly aligned during the clutter measurements.

3.4 Roadside Object RCS Measurements

The roadside object radar cross-section measurements were performed at three polarizations, HH, VV and VH. The radar cross-section was measured at two distances, $R_{tar} = 12$ and 16 m. The guard rail RCS was measured at $R_{tar} = 15$ and 20 m, to avoid receiver saturation. Figure 3.3 is a block diagram of the experiment setup.

The measured object was mounted upright on the 1.2 m diameter turntable. The radar system transmitter and receiver were mounted on a tripod, at a height $h = 1.395$ m. At this height, the Tx and Rx antennas are centered on the object length $L = 88.9$ cm. The target area illuminated increases when the target distance R_{tar} increases. The length d , in Figure 3.3, is the length of target illuminated by the Tx and Rx antennas. The object length L was designed to be much larger than the length d . For the largest target distance, $R_{tar} = 20$ m, the illuminated length d is

59.4 cm. Therefore, only the object is being illuminated, and any edge effects are minimal.

The received voltage from the radar system was sampled and stored during one complete scan of the object. The object was rotated in a clock-wise direction. The measurement was performed at least twice, for each polarization and target distance.

The required sample rate, during the object scan, is an important consideration. Enough samples should be taken to adequately profile the object shape. The number of samples decided upon was $M = 425$. With $M = 425$ samples, the object RCS profile was measured in 0.847° increments. The required sample rate SR_1 , was then computed from the turntable scan rate $\omega = 0.2617$ rad/sec, and $M = 425$ samples. The result is $SR_1 = 17.618$ samp/sec. The RCS measurement results, presented in Chapter 6, clearly profile each object shape. Thus, the choice of $M = 425$ samples was more than adequate.

To perform system calibration, the radar system and corner reflector were moved to one side of the turntable. The corner reflector was then placed at the same distance as the roadside object ($R_{cr} = R_{tar}$). The antennas were then properly aligned, and the received voltage recorded. The radar system was then moved in front of the turntable, and the data acquisition started.

Chapter 4

Data Analysis

This following chapter develops and presents the equations used in the data analysis. The mono-static radar range equation is used to compute the surface clutter and the roadside object radar cross-section. The monostatic equation used in radar system calibration is discussed.

The probability density characteristics of the received power are also discussed. For both surface clutter and roadside objects, a normalized CDF is computed from the sample data. The surface clutter and roadside object experimental CDF results are compared to both a Rayleigh and Weibull distributed CDF function.

4.1 Surface Clutter Normalized RCS

The surface clutter is represented in terms of normalized radar cross-section (RCS), also referred to sigma-zero. Sigma-zero, or σ^o , is defined in Equation 4.1, where σ is the measured RCS and A_e is the surface area illuminated by the antenna.

$$\sigma^o = \frac{\sigma}{A_e} \quad (4.1)$$

Sigma-zero is a dimensionless quantity that is independent of the area illuminated by the antenna.

Average sigma-zero values, or $\overline{\sigma^0}$, are computed from experimental data. First, the received voltage data from the radar scan is converted to power values from the log amplifier calibration curve. This results in a power value, P_{Ra} , for each sample. The mean power value, $\overline{P_{Ra}}$, is computed from N samples of P_{Ra} :

$$\overline{P_{Ra}} = \frac{1}{N} \sum_{i=1}^N P_i \quad (4.2)$$

The normalized RCS, $\overline{\sigma^0}$, is computed from the monostatic radar range equation [10]. The unknown parameter in Equation 4.3 is $\overline{\sigma^0}$:

$$\overline{P_{Ra}} = \frac{P_t G_r G_t \lambda^2 \overline{\sigma^0} A_e}{64 \pi^3 R_a^4} A_{sys} \quad (4.3)$$

Expressing Equation 4.3 with $\overline{P_{Ra}}$ as the dependent variable simplifies the calibration discussion. The area illuminated A_e , is calculated from Equation 4.4, assuming a beamwidth-limited antenna footprint. The distance to the surface R_a , was previously defined in Chapter 3, Equation 3.3.

$$A_e = \frac{\pi R_a^2 \Theta_{BW}^2}{4 \sin(\Theta_d)} \quad (4.4)$$

The total system gain, A_{sys} , takes into account amplifier gain and cable loss in the radar system. A_{sys} is approximately 37.5 dB, but is not known exactly. A_{sys} can be eliminated from Equation 4.3 by system calibration. The received power from the calibration target is expressed in Equation 4.5, where σ_{cr} is the corner reflector RCS:

$$P_{Rcr} = \frac{P_t G_r G_t \lambda^2 \sigma_{cr}}{64 \pi^3 R_{cr}^4} A_{sys} \quad (4.5)$$

Equation 4.5 is the monostatic radar range equation for a point target. All parameters in equation 4.5 are known, except A_{sys} . The system gain is eliminated by dividing Equation 4.3 by Equation 4.5. Solving for $\overline{\sigma^o}$, the result is given by Equation 4.6:

$$\overline{\sigma^o} = \frac{\sigma_{cr} \overline{P_{Ra}} R_a^4}{A_e \overline{P_{Rcr}} R_{cr}^4} \quad (4.6)$$

The tetrahedral corner reflector RCS, σ_{cr} , is not known for cross polarizations. Therefore, this calibration procedure only applies to the co-polarized sigma-zero measurements. The VV and HH sigma-zero results are referred to as $\overline{\sigma_{VV}^o}$ and $\overline{\sigma_{HH}^o}$. The $\overline{\sigma_{VH}^o}$ is obtained using the ratio of VH mean power and the co-polarized mean power, multiplied by the co-polarized sigma-zero value. The VH average sigma-zero value, $\overline{\sigma_{VH}^o}$ is given in Equation 4.7:

$$\overline{\sigma_{VH}^o} = \frac{\overline{\sigma_{VV,HH}^o} \overline{P_{Ra}|VH}}{\overline{P_{Ra}|VV,HH}} \quad (4.7)$$

There are two $\overline{\sigma_{VH}^o}$ values, one each from the VV and the HH results. The overall $\overline{\sigma_{VH}^o}$ is an average of both the above values.

An average sigma-zero value is obtained for each radar scan. From six radar scans at each polarization, an overall mean sigma-zero value is calculated. Equation 4.6 shows the co-pol mean value dependence on the calibrated power value. A separate experiment was performed to calculate the calibration power, or P_{Rcr} , accuracy. The measured P_{Rcr} values typically varied between $\pm 15\%$ of the average value. The overall mean sigma-zero accuracy is estimated from minimum and maximum P_{Rcr} values and the $\overline{\sigma^o}$ values obtained from each scan. The cross-pol mean sigma-zero value accuracy is determined from previously computed minimum and maximum co-pol average values. The mean sigma-zero value, $\langle \overline{\sigma^o} \rangle$, and $\langle \overline{\sigma_{VH}^o} \rangle$ for cross-pol, and the accuracy estimate, are presented in Chapter 5.

4.2 Roadside Object RCS

The radar cross-section of the roadside objects was measured at several target distances, for VV, HH and VH polarizations. The amount of target area illuminated changes with target distance, because the antenna beamwidth changes with distance. The illuminated target area is also changed when rotating the target during the sampling process. Computation of the illuminated target area is not possible because of the complex target shape and the aspect angle dependence [16].

Therefore, the roadside objects must be assumed to be a point target. For a point target, the measured RCS is referred to as σ with units of square meters. A σ value is computed from each sample point. A target scattering profile can thus be measured, by plotting the σ values versus aspect angle.

The radar range equation for a point target is given in Equation 4.8. Equation 4.8 is written in terms of the received power, $P_{R_{tar}}$ to simplify the system calibration discussion. $P_{R_{tar}}$ is the measured value in Equation 4.8:

$$P_{R_{tar}} = \frac{P_t G_r G_t \lambda^2 \sigma}{64 \pi^3 R_{tar}^4} A_{sys} \quad (4.8)$$

The radar range equation used in system calibration was previously given in Equation 4.5. The system gain, A_{sys} , is eliminated by dividing Equation 4.8 by Equation 4.5. The target distance R_{tar} , is equal to the distance from the calibration target R_{cr} , so both can be eliminated. Solving for σ , the result is given by Equation 4.9:

$$\sigma = \frac{\sigma_{cr} P_{R_{tar}}}{P_{R_{cr}}} \quad (4.9)$$

Co-polarized sigma values, for each aspect angle, are presented in a polar plot. The average power value, $\overline{P_{R_{tar}}}$, is computed from the target scan and used to compute the average sigma value. The average sigma value, $\overline{\sigma}$, is computed from Equation 4.10:

$$\overline{\sigma} = \frac{\sigma_{cr} \overline{P_{R_{tar}}}}{P_{R_{cr}}} \quad (4.10)$$

It was not possible to compute the cross polarization RCS, σ_{VH} , at each target aspect angle. The average cross-pol sigma value, $\overline{\sigma_{VH}}$, can be computed from the average co-polarized values. Equation 4.11 is used to compute $\overline{\sigma_{VH}}$:

$$\overline{\sigma_{VH}} = \frac{\overline{\sigma_{VV,HH}} \overline{P_{R_{tar}}|_{VH}}}{\overline{P_{R_{tar}}|_{VV,HH}}} \quad (4.11)$$

The $\sigma_{VH}(avg)$ value is of both the VV and HH ratios.

The overall mean sigma values, $\bar{\sigma}$ and $\overline{\sigma_{VH}}$ for cross-pol, is estimated from three target scans. Similar to the surface measurements, the variance of $\bar{\sigma}$ is estimated from minimum and maximum $\bar{\sigma}$ values.

4.3 Radar Range Equation Parameters

The radar range equation parameters, used for both the surface clutter and roadside object measurements, are listed in Table 4.1 A brief description of each parameter is also listed. Parameters relevant only to the surface clutter equations are listed Table 4.2.

4.4 Rayleigh Distribution Comparison

The received power data, from both surface clutter and the roadside object measurements, is compared to a Rayleigh CDF. The Rayleigh distribution is commonly used to describe weather clutter and non-grazing angle surface clutter [10]. The following section will discuss the observed received power CDF and the Rayleigh distributed CDF. The observed theoretical CDF's are compared by use of the goodness-of-fit (GF) test. The GF test will also be explained in further detail.

Under the Rayleigh distribution assumption, the power output from the log amplifier is assumed to follow an exponential probability density function. This density function is obtained from a Rayleigh distributed voltage. Equation 4.12 is the

Table 4.1: Radar Range Equation Parameters

Symbol	Description	Value
P_t	Transmitted Power	40 mW (+16.02 dBm)
G_t	Tx Antenna Gain	38.8 dBi
G_r	Rx Antenna Gain	38.6 dBi
λ	Wavelength @95 GHz	3.158 mm
σ_{cr}	Corner Reflector RCS	159.99 m^2
A_{sys}	Radar System Gain	≈ 37.5 dB
Θ_{BW}	3 dB Beamwidth	1.7° (0.0297 rad)

Table 4.2: Surface Clutter Parameters, at 7.5° and 5.0°

Symbol	Description	Value	
Θ_d	Depression Angle	7.5°	5.0°
R_a	Range to Surface	12.03 m	18.01 m
A_e	Illuminated Area	0.767 m^2	2.573 m^2

Rayleigh voltage PDF, with voltage v , and mean voltage estimate V .

$$p(v) = \frac{2v}{V^2} \exp\left(-\frac{v^2}{V^2}\right) \quad v \geq 0 \quad (4.12)$$

The Rayleigh power PDF is obtained by substituting x for v^2 . Equation 4.13 is the exponential power PDF, with X_o as the average power.

$$p(x) = \frac{1}{X_o} \exp\left(-\frac{x}{X_o}\right) \quad x \geq 0 \quad (4.13)$$

Equation 4.13 is rewritten in terms of the mean estimate b , where $b = X_o$. Equation 4.14 is the result:

$$p(x) = \frac{1}{b} \exp\left(\frac{-x}{b}\right) \quad x \geq 0 \quad (4.14)$$

A Rayleigh normalized power CDF function is derived from Equation 4.14, assuming the estimated mean is normalized. The Rayleigh normalized power CDF is given by Equation 4.16:

$$P(x) = \int_0^x p(y) dy \quad (4.15)$$

$$P(x) = 1.0 - \exp(-x) \quad b = 1.0 \quad (4.16)$$

The experimental normalized CDF is computed from the sampled data. First, each power sample P_i , is divided by the mean power value $\overline{P_i}$. The normalized values are then ordered from smallest to the largest to form x_i . The parameter x_i is defined by Equation 4.17:

$$x_i = \text{Ordered} \left[\frac{(P_i)}{(\overline{P_i})} \right] \quad (4.17)$$

The mean power value $\overline{P_i}$, was previous defined in Equation 4.2. The experimental normalized CDF $F(x_i)$ can then be determined from the ordered samples. Equation 4.18 defines the $F(x_i)$ parameter:

$$F(x_i) = \frac{i}{N} \quad i = 1 \text{ to } N \quad (4.18)$$

Each $F(x_i)$ value is compared to a corresponding theoretical CDF value. The theoretical CDF $P(x_i)$, is found by evaluating Equation 4.15 at $x = x_i$. The resulting $P(x_i)$ is given by Equation 4.19:

$$P(x_i) = 1.0 - \exp(-x_i) \quad (4.19)$$

The GF test was used to compare the $F(x_i)$ and $P(x_i)$. The GF test is performed by computing a test statistic value from experimental and theoretical values. The test statistic χ^2 follows a chi-squared distribution [14], and is found from Equation 4.20:

$$\chi^2 = \sum_{i=1}^K \frac{(o_i - e_i)^2}{e_i} \quad K = 213 \quad (4.20)$$

Where the observed value $o_i = F(x_i)$, and the expected value is $e_i = P(x_i)$. Approximately one half of the sample points, $K = 213$, were used in the GF test. Test statistic χ^2 has degree of freedom $\nu = 212$ when comparing $K = 213$ points.

The computed χ^2 is compared to χ_α^2 , where α is the test significance level. The experimental CDF matches the observed CDF with significance level α , if $\chi^2 \leq \chi_\alpha^2$. For example, a significance level $\alpha = 99.5\%$, with $\nu = 212$, has $\chi_\alpha^2 = 161.86$ [15]. The GF test results, for both the surface clutter and roadside object measurements, are presented in Chapters 5 and 6.

4.5 Weibull Distribution Comparison

The received power results are also compared to the Weibull probability distribution. The Weibull distribution best characterizes the backscatter from targets of various sizes [3]. The Weibull CDF is easily computed, and can be compared to the experimental data with minimal effort. The Ricean and log-normal distributions are also used to classify backscatter probability, but are much more difficult to compute. The GF test is again used to compare the experimental data and the Weibull CDF.

The detector output power, x , is assumed to be Weibull distributed. The Weibull PDF, is given in Equation 4.21, where b is the scale parameter and c is the shape parameter [17]. The Rayleigh and Weibull distributions are equivalent if $b = c = 1$.

$$p_w(x) = \frac{cx^{c-1}}{b^c} \exp \left\{ - \left(\frac{x}{b} \right)^c \right\} \quad x \geq 0 \quad (4.21)$$

The mean, \bar{x} , is obtained from Equation 4.22, where $\Gamma(\cdot)$ is the Gamma function.

$$\bar{x} = b \Gamma\left(1 + \frac{1}{c}\right) \quad (4.22)$$

The standard deviation, σ_x , is given by Equation 4.23:

$$\sigma_x = b \sqrt{\Gamma\left(1 + \frac{2}{c}\right) - \left\{\Gamma\left(1 + \frac{1}{c}\right)\right\}^2} \quad (4.23)$$

The Weibull CDF, $P_w(x)$, is then defined by Equation 4.25:

$$P_w(x) = \int_0^x p(y) dy \quad (4.24)$$

$$P_w(x) = 1.0 - \exp\left\{-\left(\frac{x}{b}\right)^c\right\} \quad (4.25)$$

The experimental CDF, $F(x_i)$, is obtained from the sample data. $F(x_i)$ was previously defined in Equation 4.17. The normalized Weibull CDF, $P_w(x_i)$, is compared to $F(x_i)$ by using the goodness-of-fit test. $P_w(x_i)$ is computed from Equation 4.26:

$$P_w(x_i) = 1.0 - \exp\left\{-\left(\frac{x_i}{\hat{b}}\right)^{\hat{c}}\right\} \quad (4.26)$$

Where \hat{b} and \hat{c} are the estimated normalized Weibull CDF scale and shape parameters. The parameters \hat{b} and \hat{c} are computed from the parameter f . Equation 4.27 is used to compute f , with Var as the normalized power sample variance [18]:

$$f = \frac{1}{1 + Var} \quad (4.27)$$

A Gamma function approximation, shown in Equation 4.28, is also required.

$$\frac{[\Gamma(1 + z)]^2}{\Gamma(2 + z)} \approx 1 - 0.5z^{1.2203} \quad (4.28)$$

The approximation for z is then computed by Equation 4.29:

$$z = 2(2 - f)^{1/1.2203} \quad (4.29)$$

The \hat{b} and \hat{c} parameters now can be computed:

$$\hat{c} = \frac{1}{z} \quad \hat{b} = \frac{1}{\Gamma(1 + z)} \quad (4.30)$$

The goodness-of-fit test for $F(x_i)$ and $P_w(x_i)$ was performed using $M = 213$ sample points. Comparison between the experimental and Weibull CDF's is discussed in Chapters 5 and 6. The goodness-of-fit test results and normalized power variance values are listed for both the surface clutter and roadside object measurements.

Chapter 5

Surface Clutter Measurements

Grazing angle clutter measurements, for five different surfaces, are presented in this chapter. Surface clutter was measured at grazing angles of 7.5° and 5.0° , and at VV, HH and VH polarization combinations. The five surfaces measured are asphalt, gravel, new snow, grass, and bare soil. Data for each surface are presented in a separate section. The average sigma-zero, or $\langle \sigma^o \rangle$ values, are listed at both grazing angles and for all polarizations.

The received power statistics are also considered. The normalized power variance and the maximum normalized power values are listed for each surface. For all the surfaces considered, the normalized power CDF best matches the Rayleigh distribution. Therefore, the Weibull distribution \hat{b} and \hat{c} parameters are not listed. The goodness-of-fit test results, for both Rayleigh and Weibull distributions, are listed in each section.

5.1 Asphalt Parking Lot

The first surface considered is an asphalt parking lot. A dry, flat section of asphalt was chosen for the experiment. The surface had an estimated height variation of

± 0.75 cm. A photo of the surface is included in Appendix B, Figure B.1. A summary of surface conditions is also provided in Appendix B.

The experimental sigma-zero results are listed in Table 5.1. The average sigma-zero values are quite low. From the Rayleigh roughness criteria, with $\Delta h = 1.5$ cm, the asphalt surface is considered rough when $\Theta_g \geq 1.51^\circ$. The measurements at 5.0° are near the radar system minimum detectable signal level. This would cause the measured experimental average to be slightly higher than the actual value. At both grazing angles, the HH and VV average values are almost identical. At 7.5° grazing, the VH sigma-zero value is only 1.0 to 1.5 dB lower than the co-polarized results. Comparing the 5.0° and 7.5° results, the VV, HH and VH average sigma-zero value decreases when the grazing angle is reduced.

The asphalt sigma-zero results differ from those presented by Yamaguchi et al. [4]. The VV, HH and VH measurements at 7.5° are approximately 4.0 dB higher than Yamaguchi's measurements. At 5.0° grazing, the experimental VV, HH and VH average sigma-zero values are 3.0 to 4.0 dB lower than Yamaguchi's results. Little ground truth information is provided with the results. Slightly different results could be attributed to surface irregularities. Also, no measurement error estimates were provided.

Table 5.1: Asphalt Sigma-zero Results

Pol.	$\langle \sigma^0 \rangle$ (dB), at 7.5°	$\langle \sigma^0 \rangle$ (dB), at 5.0°
VV	-18.3 ± 3.2	-26.2 ± 1.6
HH	-18.6 ± 1.6	-26.7 ± 2.1
VH	-19.7 ± 3.1	-29.7 ± 2.4

The received power statistics are listed in Table 5.2, for the 7.5° and 5.0° measurements. All experimental results match best the Rayleigh distribution. This is expected because the asphalt surface is relatively flat with uniform surface roughness. The experimental HH and VH CDF's are plotted in Figure 5.1. The HH and VH CDF plots, at 5°, show that the minimum normalized power values are not zero. For example, the VH CDF minimum x value is 0.74, The 5.0° results are clearly affected by the radar system MDS level.

Table 5.2: Asphalt Received Power Statistics

Pol.	Var.		x_{max}		χ^2 Weib.		χ^2 Ray.	
	7.5°	5.0°	7.5°	5.0°	7.5°	5.0°	7.5°	5.0°
VV	0.92	0.23	3.49	4.40	34.95	38.08	0.68	10.37
HH	0.86	0.23	4.37	3.04	31.45	37.20	0.92	13.14
VH	1.57	0.18	4.94	2.76	33.80	38.72	3.03	21.33

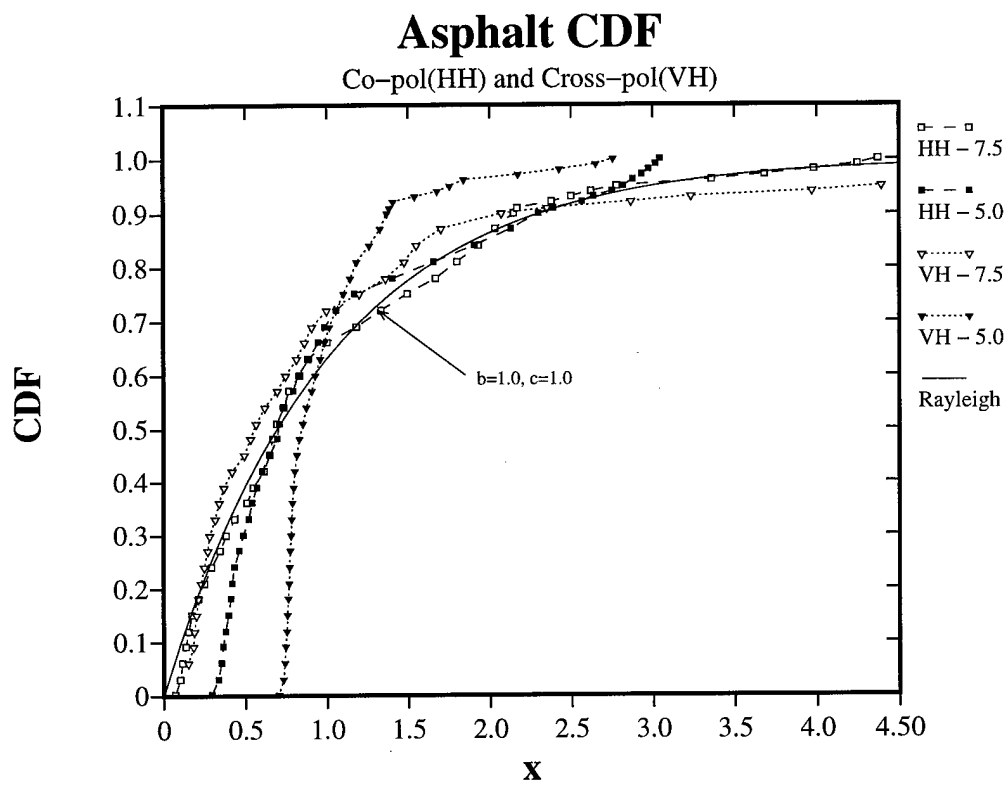


Figure 5.1: Asphalt CDF, at 7.5° and 5.0°

5.2 Gravel Parking Lot

The second surface considered is a gravel parking lot. Average sigma-zero results were obtained from both wet and dry gravel. The wet measurements were collected immediately after a heavy rainstorm. The same parking lot area was scanned so that comparison of both is possible.

A gravel surface had a height variation of ± 2.0 cm. The gravel layer thickness was approximately 22.0 cm. A table of ground truth information is included in Appendix B, Table B.2. A surface photograph is also included in Appendix B, Figure B.2.

The average sigma-zero values are listed in Tables 5.3 and 5.4, for dry and wet gravel. The wet gravel average values are approximately 5.0 to 7.0 dB lower than the dry gravel results. The surface moisture causes a reduction in signal backscatter. The scattering from a wet surface is more specular, thus causing a reduction in cross-pol. reflectivity. Complex surface scattering, due to variation in surface roughness, are also evident. The VV average sigma-zero value is slightly higher than the HH average value at 7.5° grazing. At 5.0° grazing angle, the opposite is true, i.e. the HH average is larger than the VV average sigma-zero value. This phenomenon occurs for both surface types. It is also noted that gravel has sigma-zero values ≈ 15.0 dB larger than corresponding values for asphalt. This σ° difference can be attributed to the larger gravel surface roughness conditions.

The received power statistics, for both surface types, are listed in Tables 5.5 and 5.6. The normalized power variance is slightly larger, at all polarizations, for the wet surface. Wet gravel also has larger maximum normalized power values. The wet surface causes higher variation in the received power. The wet and dry surfaces have similar goodness-of-fit test statistics. All measurements best match the Rayleigh distribution.

Table 5.3: Dry Gravel Sigma-zero Results

Pol.	$\langle \overline{\sigma^0} \rangle$ (dB), at 7.5°	$\langle \overline{\sigma^0} \rangle$ (dB), at 5.0°
VV	-1.2 ± 1.6	-11.3 ± 1.4
HH	-1.9 ± 1.4	-9.3 ± 1.5
VH	-14.7 ± 2.1	-25.7 ± 1.7

Table 5.4: Wet Gravel Sigma-zero Results

Pol.	$\langle \overline{\sigma^0} \rangle$ (dB), at 7.5°	$\langle \overline{\sigma^0} \rangle$ (dB), at 5.0°
VV	-7.7 ± 2.3	-19.1 ± 1.3
HH	-11.0 ± 2.1	-15.0 ± 3.0
VH	-21.9 ± 1.5	-27.9 ± 1.4

The HH and VH experimental CDF curves are plotted in Figures 5.2 and 5.3. The experimental curves follow the Rayleigh distribution very closely. In both dry and wet gravel plots, the 5.0° grazing angle results are affected by the system noise level. The wet gravel is more affected, because lower backscatter occurs from the surface.

Table 5.5: Dry Gravel Received Power Statistics

Pol.	Var.		x_{max}		χ^2 Weib.		χ^2 Ray.	
	7.5°	5.0°	7.5°	5.0°	7.5°	5.0°	7.5°	5.0°
VV	0.80	1.00	4.09	3.84	28.94	29.14	0.31	0.75
HH	0.65	0.66	3.55	3.52	29.27	32.17	0.95	2.49
VH	0.76	0.38	3.99	3.23	30.49	34.49	0.94	7.09

Table 5.6: Wet Gravel Received Power Statistics

Pol.	Var.		x_{max}		χ^2 Weib.		χ^2 Ray.	
	7.5°	5.0°	7.5°	5.0°	7.5°	5.0°	7.5°	5.0°
VV	1.90	1.06	5.56	4.04	29.63	28.34	3.97	0.54
HH	0.87	0.86	4.93	4.16	31.23	27.54	0.77	1.04
VH	0.68	0.59	3.05	3.67	32.23	35.42	2.37	6.35

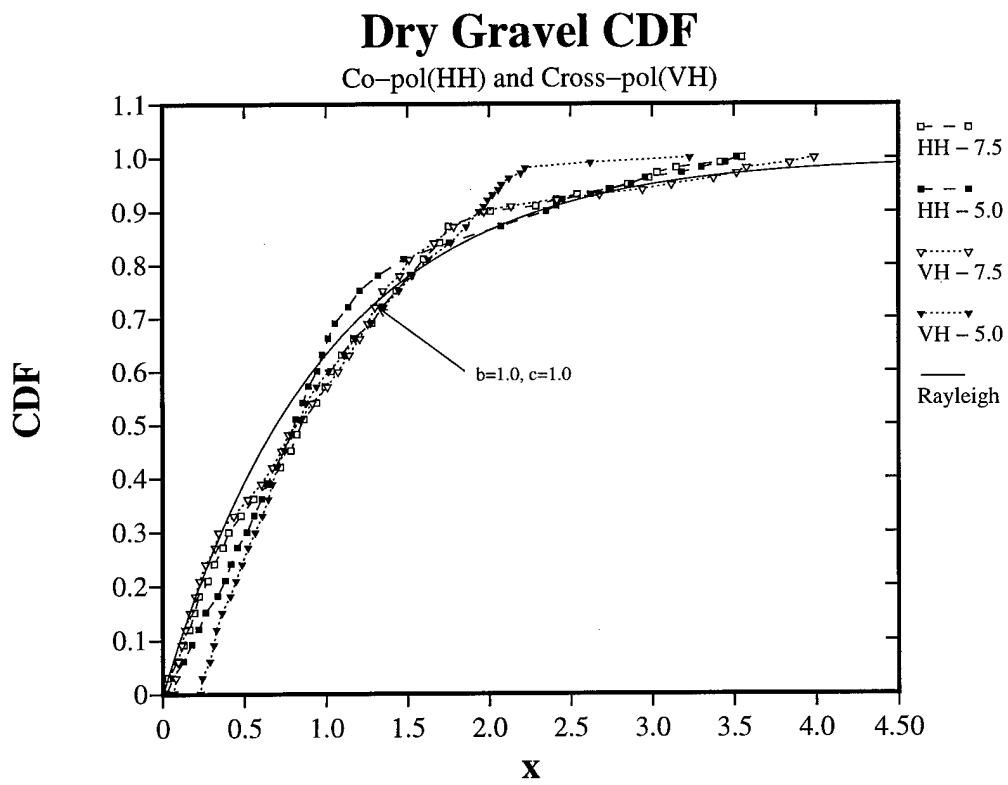


Figure 5.2: Dry Gravel CDF, at 7.5° and 5.0°

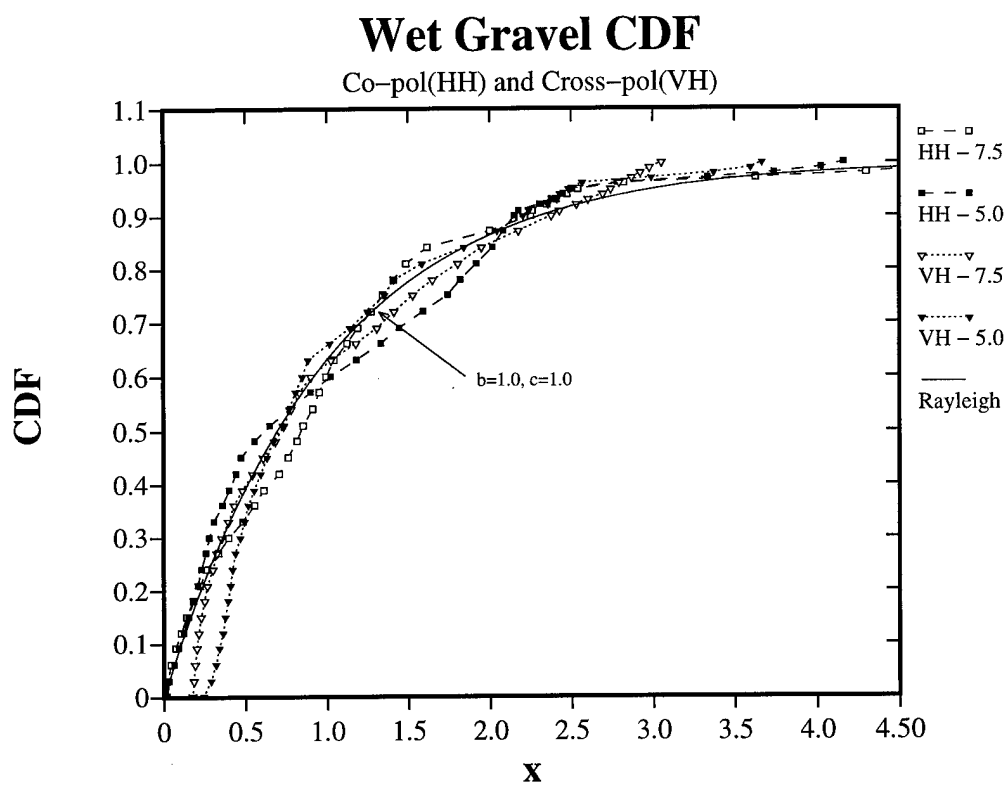


Figure 5.3: Wet Gravel CDF, at 7.5° and 5.0°

5.3 Dry Snow Results

The next surface measured was dry snow. There are three basic types of snow: dry, wet and refrozen snow. Each type has different reflective properties, because of moisture content, surface conditions and snow depth. Scattering from a snow surface is further complicated when considering the penetration depth of the transmitted waveform. At millimeter wavelengths, it can be assumed that the penetration depth is small.

The snow data presented in this section are from dry snow. Several unsuccessful attempts were made to measure refrozen and wet snow. Equipment was not available to measure the snow liquid water content. This limited the snow measurements to the extreme cases, either all dry, all wet or all refrozen snow. For the dry snow experiment, the snow had fallen the day before, and the temperature was 10° F during the data collection. The experimental surface photograph is included in Appendix B, Figure B.3. A list of ground truth information is also included in Appendix B.

The dry snow data average values are shown in Table 5.7. The HH polarization values are slightly higher than the VV pol. values at both 7.5° and 5.0° grazing angle. For all polarizations, the average sigma-zero value decreases when the grazing angle is decreased. The Georgia Tech clutter model results are listed in Table 5.8. Direct comparison of the dry snow results to the clutter model is not possible. The Georgia Tech clutter model only applies to wet and refrozen snow. However, the clutter model appears to underestimate the effect of changes in grazing angle. From our dry snow measurements, a 2.5° change in grazing angle, from 7.5° to 5.0°, resulted in a 11 to 12 dB change in the average sigma-zero value. The Georgia Tech clutter model, however, suggests only a 2 dB difference in sigma-zero, between 7.5° and 5.0°. It is suggested that this discrepancy is caused by inappropriate data extrapolation.

Table 5.7: Dry Snow Sigma-zero Results

Pol.	$\langle \overline{\sigma^0} \rangle$ (dB), 7.5°	$\langle \overline{\sigma^0} \rangle$ (dB), 5.0°
VV	-4.7 ± 1.0	-17.1 ± 1.4
HH	-4.3 ± 0.8	-15.6 ± 2.7
VH	-17.9 ± 1.4	-25.5 ± 1.5

Table 5.8: Clutter Model, VV or HH Sigma-zero Results

Wet Snow		Refrozen Snow	
$\langle \overline{\sigma^0} \rangle$ (dB), 7.5°	$\langle \overline{\sigma^0} \rangle$ (dB), 5.0°	$\langle \overline{\sigma^0} \rangle$ (dB) 7.5°	$\langle \overline{\sigma^0} \rangle$ (dB), 5.0°
-13.99	-15.95	-6.85	-8.81

The dry snow received power statistics are listed in Table 5.9. At 7.5° grazing angle, the VV and HH normalized power statistics are slightly different. The VV pol. has a higher variance and larger maximum normalized power value (x_{max}). The VV and HH statistics are almost identical at 5.0° grazing. However, all VV and HH results still match best to the Rayleigh CDF assumption.

The HH and VH experimental CDF's are plotted in Figure 5.4. The VH values again appear to be affected by the radar system noise level. The VH CDF values still match the Rayleigh CDF to a reasonable significance level.

Table 5.9: Dry Snow Received Power Statistics

Pol.	Var.		x_{max}		χ^2 Weib.		χ^2 Ray.	
	7.5°	5.0°	7.5°	5.0°	7.5°	5.0°	7.5°	5.0°
VV	1.63	0.71	5.99	3.62	35.10	30.09	3.96	0.71
HH	0.88	0.78	4.08	3.92	29.22	29.32	0.14	0.52
VH	0.62	0.46	3.91	3.31	35.11	35.51	11.14	7.68

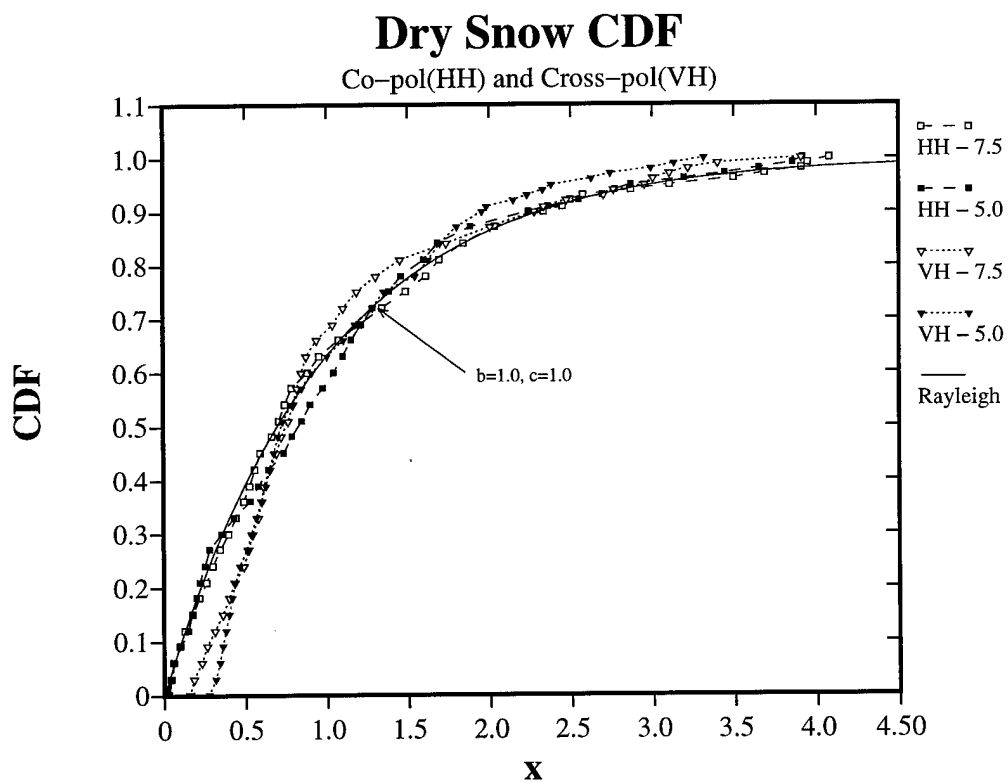


Figure 5.4: Dry Snow CDF, at 7.5° and 5.0°

5.4 Dry Soil Results

The next surface considered is dry, bare soil. The research site selected was a newly planted soybean field. The data were collected before any vegetation was present. A surface photo is included in Appendix B, Figure B.4. The ground truth information is also listed in Appendix B, Table B.4. The estimated surface roughness was approximately ± 3.5 cm. Irrigation of the field was not possible, and rainfall did not occur while the field was still vegetation free. Thus, wet soil measurements were not obtained for comparison.

Considering the Rayleigh scattering criteria, the soil surface has a height variation $\Delta h = 7.0$ cm. The soil surface is considered “rough” at grazing angles $\geq 0.30^\circ$. The 7.5° and 5.0° grazing angles are far from the “smooth” grazing angle condition.

The experimental results are listed in Table 5.10. At both 7.5° and 5.0° , the VV and HH average values are very similar. The VH average sigma-zero values are approximately 10 dB lower than the co-pol. average values. For all polarizations, the average value decreases when decreasing the grazing angle.

Table 5.10: Dry Soil Sigma-zero Results

Pol.	$\langle \sigma^0 \rangle$ (dB), at 7.5°	$\langle \sigma^0 \rangle$ (dB), at 5.0°
VV	-7.2 ± 1.4	-14.2 ± 1.2
HH	-7.9 ± 1.4	-14.9 ± 1.1
VH	-16.8 ± 2.0	-24.6 ± 2.4

The received power statistics are listed in Table 5.11. The VV and HH polarization results have similar variance and χ^2 test results. Again, the experimental data best matches the Rayleigh distribution. The HH and VH experimental CDF's are plotted

in Figure 5.5. At 5.0° grazing, the HH and VH CDF plots appears to vary around the Rayleigh CDF plot. The VH CDF plot at 5.0° is affected slightly by the radar system noise level. Thus, the calculated average VH sigma-zero at 5.0° is slightly larger than the actual value.

Table 5.11: Dry Soil Received Power Statistics

Pol.	Var.		x_{max}		χ^2 Weib.		χ^2 Ray.	
	7.5°	5.0°	7.5°	5.0°	7.5°	5.0°	7.5°	5.0°
VV	0.86	1.06	4.12	4.77	27.62	28.57	0.66	0.69
HH	0.74	0.65	4.47	3.37	32.67	26.12	1.90	1.38
VH	0.82	0.79	4.18	4.80	31.33	37.04	0.78	6.92

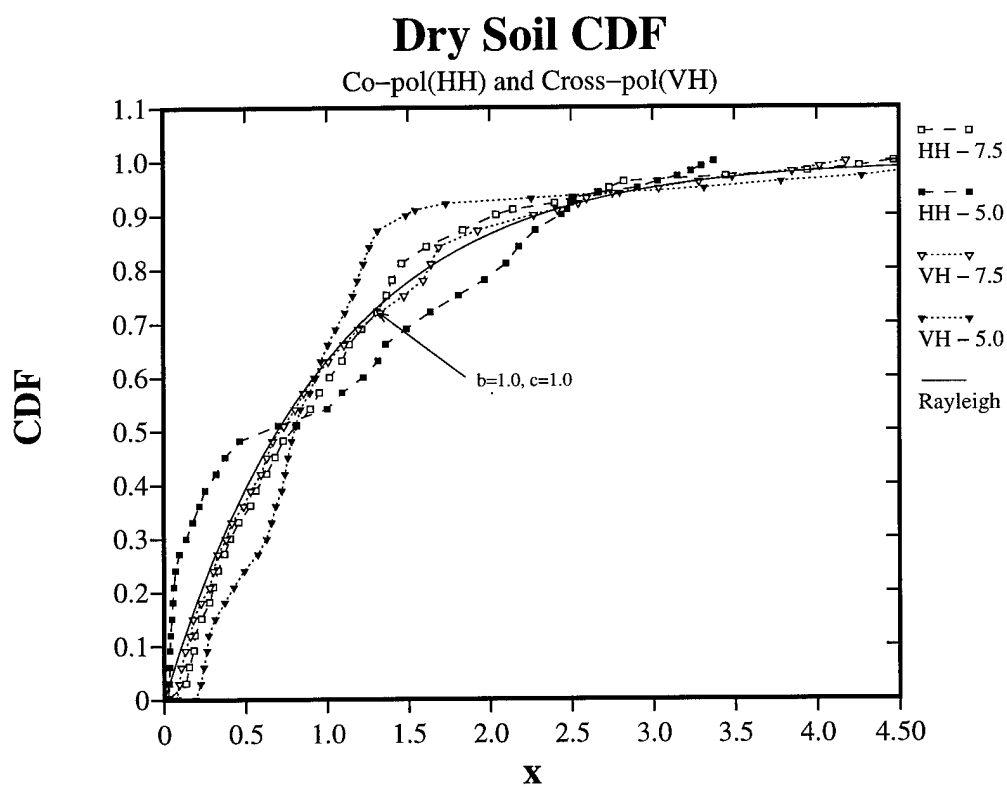


Figure 5.5: Dry Soil CDF, at 7.5° and 5.0°

5.5 Grass Surface Results

The final surfaces considered are tall and short grass. The results for both grass types will be compared. A measure of sigma-zero variability, due to different conditions, is possible from the comparison. Short, dormant grass, with height of 3.5 cm and surface variation of ± 2.0 cm, was measured during early spring. The same grass field was measured two months later. The grass had grown to a height of 9.0 cm, with a surface height variability of ± 3.5 cm. From the Rayleigh scattering model, the tall grass surface is considered "rough" at grazing angles $\geq 0.32^\circ$. The short grass surface is "rough" at $\geq 0.57^\circ$ grazing. Photographs of both surfaces are included in Appendix B. The ground truth information is also provided in Appendix B, Tables B.5 and B.6.

The average sigma-zero values are listed in Tables 5.12 and 5.13. At 7.5° and 5.0° , the VV average value is higher than the HH value. This phenomenon occurs for both grass surface types. The larger VV sigma-zero values are best explained by the vertical grass stems. Also, the tall grass VV and HH average values are larger than the short grass values. Tall grass obviously has a higher specular reflection than short grass. The VH average values are very similar for both tall and short grass. This suggests that the diffuse scattering is related to factors other than grass height. The depolarization scattering effect is perhaps related to the underlying soil, since the grass VH values are similar to the bare soil results. The overall sigma-zero variation, caused by the different grass conditions, is approximately 2.0 to 3.0 dB for all polarizations.

The received power statistics are also compared for both grass types. The tall grass has a larger normalized power variance, for all polarizations. This is caused by the larger tall grass surface roughness variance. The received power statistics are

Table 5.12: Short Grass Sigma-zero Results

Pol.	$\langle \overline{\sigma^0} \rangle$ (dB), at 7.5°	$\langle \overline{\sigma^0} \rangle$ (dB), at 5.0°
VV	-9.1 ± 1.1	-15.8 ± 1.1
HH	-10.1 ± 2.2	-20.0 ± 0.9
VH	-16.2 ± 2.8	-20.6 ± 2.0

Table 5.13: Tall Grass Sigma-zero Results

Pol.	$\langle \overline{\sigma^0} \rangle$ (dB), at 7.5°	$\langle \overline{\sigma^0} \rangle$ (dB), at 5.0°
VV	-6.8 ± 1.8	-13.1 ± 1.9
HH	-9.2 ± 1.2	-15.6 ± 1.3
VH	-18.0 ± 3.0	-21.8 ± 3.8

listed in Tables 5.14 and 5.15. Comparing the goodness-of-fit χ^2 test statistics, both surface types have similar values. The Rayleigh CDF is again the best match for all measurements. The short and tall grass experimental CDF's are plotted in Figures 5.6 and 5.7. The VH measurements at 7.5° are again affected by the MDS level.

Table 5.14: Short Grass Received Power Statistics

Pol.	Var.		x_{max}		χ^2 Weib.		χ^2 Ray.	
	7.5°	5.0°	7.5°	5.0°	7.5°	5.0°	7.5°	5.0°
VV	0.87	0.23	4.10	4.56	30.83	36.87	0.87	0.88
HH	0.69	0.25	4.11	3.27	31.94	30.68	1.96	1.18
VH	0.57	0.28	3.40	4.37	31.56	36.60	2.62	7.07

Table 5.15: Tall Grass Received Power Statistics

Pol.	Var.		x_{max}		χ^2 Weib.		χ^2 Ray.	
	7.5°	5.0°	7.5°	5.0°	7.5°	5.0°	7.5°	5.0°
VV	1.30	0.22	4.95	5.14	31.13	28.40	1.63	1.45
HH	0.89	0.23	3.85	4.35	27.14	30.05	0.48	0.83
VH	0.93	0.26	4.23	3.64	30.01	33.13	2.47	3.01

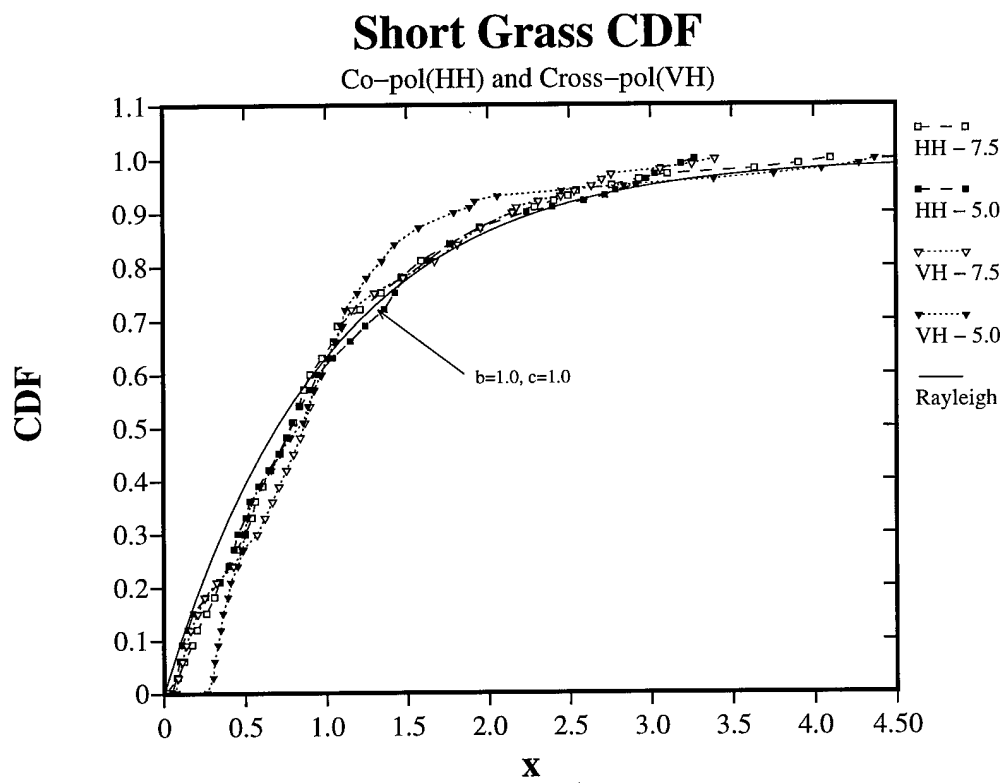


Figure 5.6: Short Grass CDF, at 7.5° and 5.0°

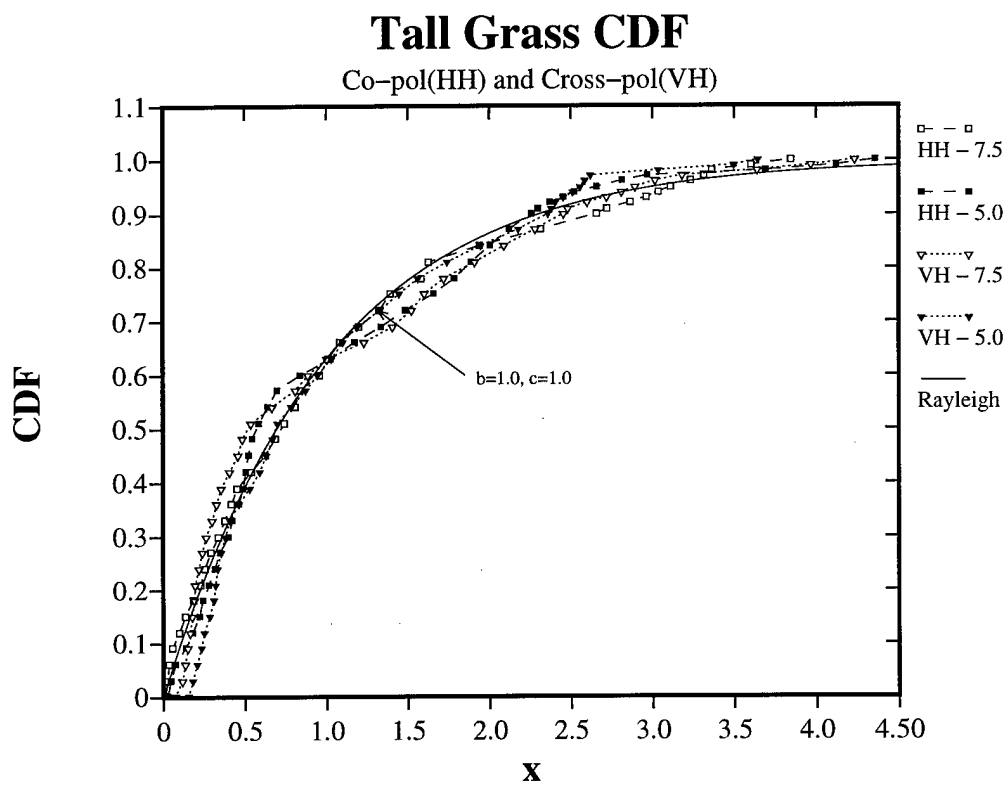


Figure 5.7: Tall Grass CDF, at 7.5° and 5.0°

Chapter 6

Roadside Object Measurements

The roadside object RCS measurements and probability statistics are presented in this chapter. Seven roadside objects were measured and the results for each are presented in a separate section. Six types of sign posts, two wood and four metal, were measured. Wood posts have gradually been replaced by metal posts because of safety requirements. A sign post is required to break away or collapse when hit, reducing the amount of damage in a collision. A section of Guard Rail was also measured. A brief description of each roadside object is included in this chapter. Photographs of the objects are included in Appendix C.

The RCS measurements were performed at ranges of 12 and 16 m. The average sigma value, $\langle\sigma\rangle$, is computed for VV, HH and VH polarizations. The VV polarization average RCS is slightly higher than the HH value. This can be attributed to the vertical orientation of the targets. A change in $\langle\sigma\rangle$, when varying the target distance, was also observed. The RCS values at 16 m are approximately 2.0 to 3.0 dB lower than the $\langle\sigma\rangle$ values at 12 m.

For VV and HH measurements, the RCS is plotted as a function of azimuth angle in a polar plot. Each polar plot includes 425 sample points. Plots of RCS are presented

only at the 12 m distance. The RCS polar plots of each target, are referenced to a top view photograph, that is included in Appendix C. It was difficult to perfectly synchronize the object scan and sampling. The experimental plot corresponds with the top photograph, to approximately $\pm 1.5^\circ$ azimuth angle. The RCS polar plots at 16 m are similar in shape to the 12 m measurements, but are reduced in value.

The received power statistics are compared to both the Weibull and Rayleigh CDF's. The experimental CDF is plotted and compared to both the Weibull and Rayleigh CDF. Changing the target distance had little effect on the received power statistics. Also, the copolarized measurements, VV and HH, have similar probability characteristics. Therefore, only the VV and VH experimental CDF's are plotted at a target distance of 12m. The estimated Weibull parameters, \hat{b} and \hat{c} are listed, as well as the variance and x_{max} of the received power values. The χ^2 goodness-of-fit test statistics, for both the Weibull and Rayleigh comparisons, are also listed. The goodness-of-fit test was performed with 213 sample points.

6.1 Round Pole, Wood

The first object measured was a round wood pole. The pole diameter is 11.1 cm (4 1/2 in). Photographs are presented in Appendix C. Round wood sign posts are still in use on major state highways. Round poles are also used to mark parking lot spaces in parking lots.

The round pole RCS, measured in dBsm, is plotted as a function of azimuth angle for VV and HH polarizations. Figure 6.1(a) and (b) show σ_{VV} and σ_{HH} at 12 m. The polar plots show a relatively uniform object shape versus azimuth angle, with variations on the order of 3 to 5 dB. The variations can be attributed to the non-uniform texture of the wood pole, which has many grooves. A uniform cylinder is

expected to have an azimuthally symmetric RCS pattern. The polar plots also show that the average σ_{HH} is smaller than σ_{VV} average. The average sigma values are listed in Table 6.1. The $\langle\sigma_{VV}\rangle$ measurements are higher than the $\langle\sigma_{HH}\rangle$ at both 12 and 16 m distances. The $\langle\bar{\sigma}\rangle$ values, for all polarizations, are reduced when increasing the target distance to 16 m.

Table 6.1: Round Wood Pole RCS Results

Pol.	$\langle\bar{\sigma}\rangle$ (dBsm), at 12m	$\langle\bar{\sigma}\rangle$ (dBsm), at 16m
VV	2.40 ± 0.7	-1.67 ± 0.8
HH	-1.12 ± 0.8	-2.82 ± 0.8
VH	-23.45 ± 3.5	-26.45 ± 1.1

The received power statistics are listed in Tables 6.2 and 6.3. The experimental CDF, for VV and VH polarizations, is plotted in Figure 6.2. The experimental CDF, for all polarizations, match both the Weibull and Rayleigh CDF rather well. However, the Rayleigh distribution is the best match for VV, HH and VH polarizations. The Rayleigh distribution is best because the normalized variance is small. The uniform pole shape results in a small normalized variance. The VH experimental CDF is effected by the radar system minimum detectable signal. For VH polarizations, the smallest x value is approximately 0.50. This causes an increase in both the χ^2 Rayleigh and χ^2 Weibull test statistics.

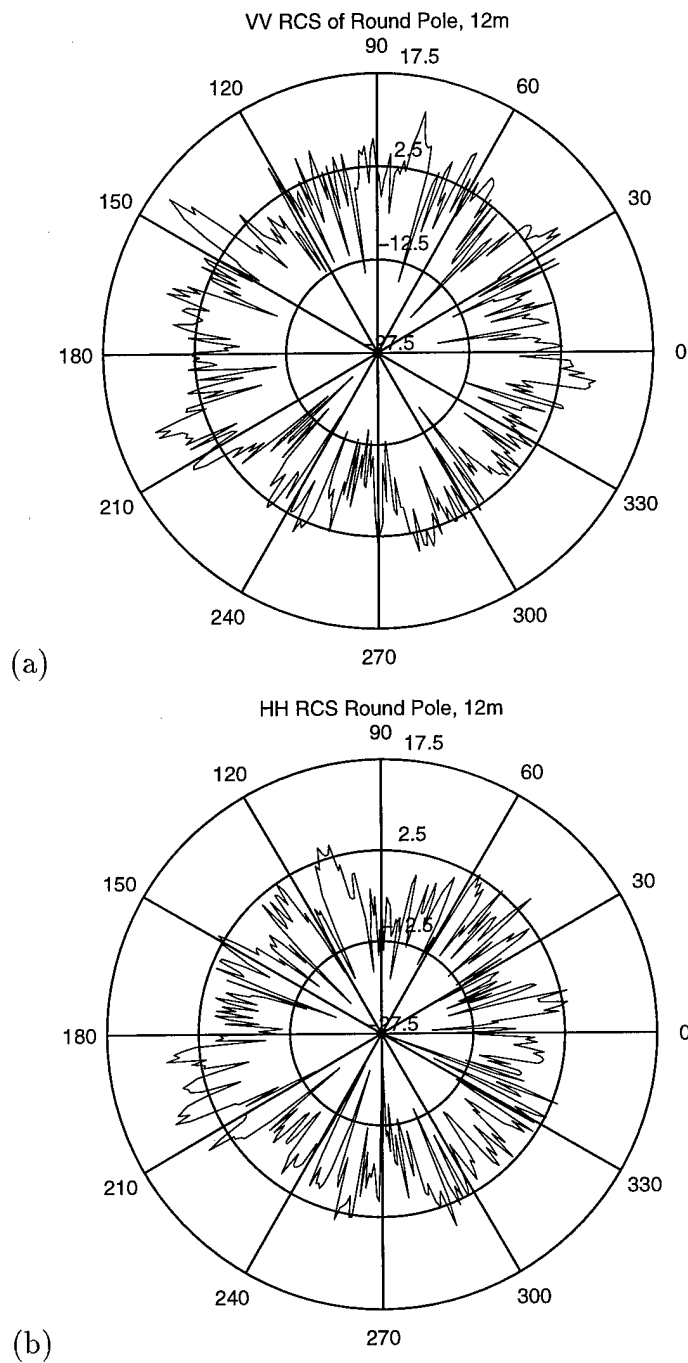


Figure 6.1: Round Wood RCS (dBsm) at 12m (a) VV Pol. (b) HH Pol.

Table 6.2: Round Pole, Received Power Statistics, 12m

Pol.	Var.	\hat{b}	\hat{c}	x_{max}	χ^2 Weib.	χ^2 Ray.
VV	2.12	0.1548	0.3270	16.60	31.06	2.56
HH	1.81	0.1655	0.3327	11.31	28.92	2.18
VH	0.30	0.3460	0.4218	3.72	38.21	16.10

Table 6.3: Round Pole, Received Power Statistics, 16m

Pol.	Var.	\hat{b}	\hat{c}	x_{max}	χ^2 Weib.	χ^2 Ray.
VV	1.78	0.1667	0.3334	9.10	27.29	5.21
HH	2.08	0.1561	0.3277	10.34	28.94	7.53
VH	0.15	0.4085	0.4525	2.83	37.54	17.57

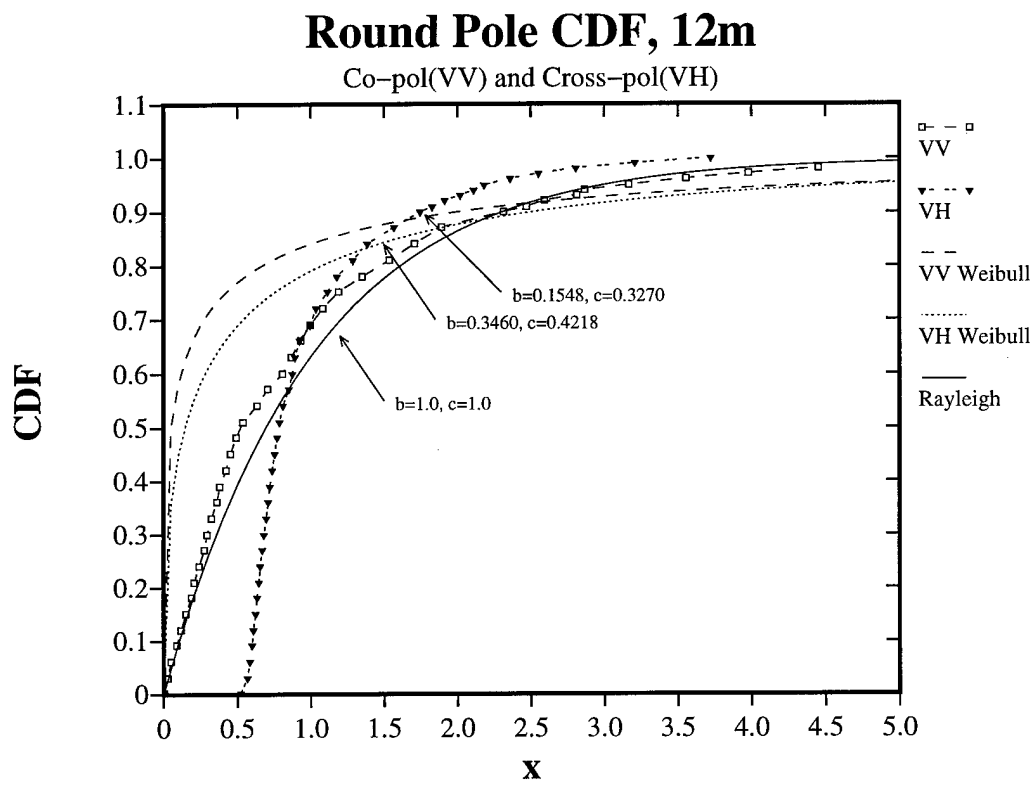


Figure 6.2: Round Wood Pole CDF, 12m

6.2 Square Pole, Wood

A square wood pole is the second measured object. Square poles are still used for road signs on state and county highways. The pole dimensions are 8.73 cm x 8.73 cm (3 7/16 in x 3 7/16 in). Figures C.3 and C.4, in Appendix C, show the square pole top and side view.

The square pole RCS, for σ_{VV} and σ_{HH} , is plotted in Figures 6.3(a) and (b). The square pole RCS is minimum at the corners, and maximum at each square face. Four peaks, separated by 90° , are clearly seen in the polar plots. The average RCS values, for VV, HH and VH polarizations are listed in Table 6.4. The VV average sigma is higher than the HH average sigma value at both 12 and 16 m. The co-pol $\langle \bar{\sigma} \rangle$ values are reduced when increasing the target distance. The measured VH $\langle \bar{\sigma} \rangle$ value is larger at 16 m than at 12 m. The cross-pol reflectance is very low, causing the radar system MDS level to affect the average VH values.

Table 6.4: Square Wood Pole RCS Results

Pol.	$\langle \bar{\sigma} \rangle$ (dB), at 12m	$\langle \bar{\sigma} \rangle$ (dB), at 16m
VV	-0.412 ± 0.8	-4.92 ± 1.3
HH	-4.79 ± 0.8	-7.08 ± 1.4
VH	-25.56 ± 2.1	-24.49 ± 1.1

The received power statistics are listed in Tables 6.5 and 6.6. The experimental CDF is plotted, along with the estimated Weibull and Rayleigh CDF in Figure 6.4. The square pole shape causes the VV and HH normalized variance to be large. The VV and HH CDF results best match the Weibull distribution. The VH power variance is abnormally low because the received signal is near the system noise level. Overall,

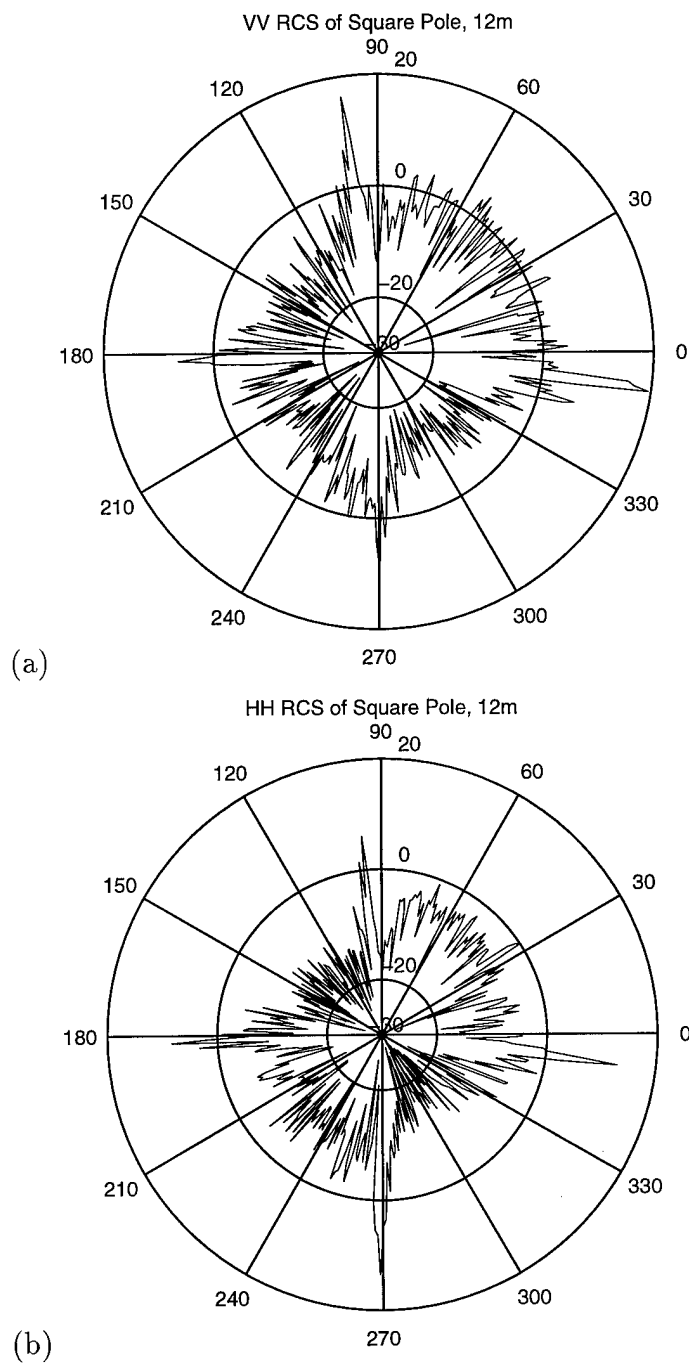


Figure 6.3: Square Wood Pole RCS (dBsm) at 12m (a) VV Pol. (b) HH Pol.

the experimental VH CDF best matches the Rayleigh distribution. However, the VH CDF tail, at $x \geq 1.25$, best follows the Weibull distribution.

Table 6.5: Square Pole Power Statistics, 12m

Pol.	Var.	\hat{b}	\hat{c}	x_{max}	χ^2 Weib.	χ^2 Ray.
VV	39.76	0.0867	0.2862	113.67	20.81	165.78
HH	16.67	0.0924	0.2901	57.1	22.68	82.45
VH	0.8406	0.2336	0.3674	10.67	82.92	29.8

Table 6.6: Square Pole Power Statistics, 16m

Pol.	Var.	\hat{b}	\hat{c}	x_{max}	χ^2 Weib.	χ^2 Ray.
VV	30.65	0.0879	0.2870	92.47	22.22	122.23
HH	16.87	0.0923	0.2901	62.49	23.39	90.48
VH	0.9354	0.2227	0.3620	17.91	43.28	34.69

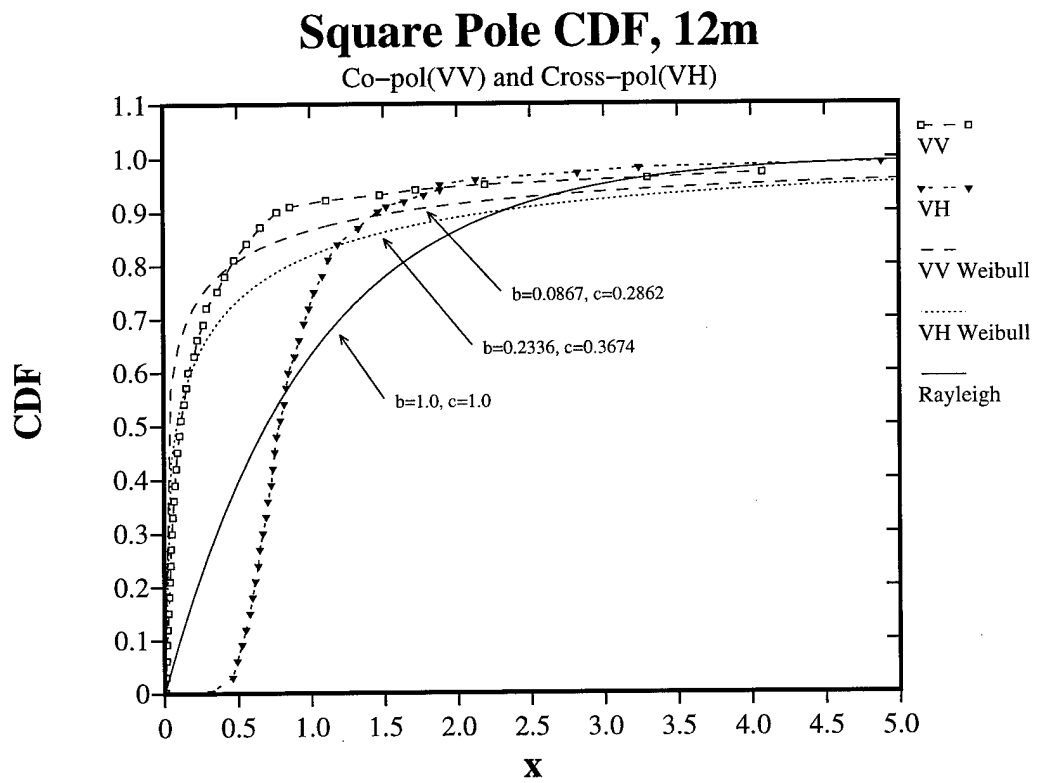


Figure 6.4: Square Wood Pole CDF, 12m

6.3 I-Beam Post, Metal

The third target measured is a metal I-Beam post. An I-Beam post is used for larger road signs, and are typically found on interstate highways. The I-Beam is rectangular shaped, with dimensions 4.9 cm x 4.15 cm (2 in x 1 5/8 in). I-Beam post photographs are included as Figures C.5 and C.6, in Appendix C.

The I-Beam RCS, for σ_{VV} and σ_{HH} , are plotted in Figure 6.5(a) and (b). The VV and HH polar plots are very similar. The maximum σ occurs at each rectangular face. Four maximum values, separated by 90° , can be seen in the polar plots. The metal I-Beam post has larger values between maxima, when comparing the plots to the square wood pole results. The metal is much more reflective than wood. Broader lobes between maxima also occur, because of the channel I-Beam shape. This channel shape is similar to a tetrahedral corner reflector. The $\langle \sigma_{VV} \rangle$ is slightly higher than the $\langle \sigma_{HH} \rangle$ value. The average RCS values, at 12 and 16 m, are listed in Table 6.7. The average RCS values are again lower at 16 m.

Table 6.7: I-Beam RCS Results

Pol.	$\langle \bar{\sigma} \rangle$ (dBsm), at 12m	$\langle \bar{\sigma} \rangle$ (dBsm), at 16m
VV	12.29 ± 1.9	9.70 ± 0.8
HH	11.32 ± 0.7	8.02 ± 0.9
VH	-17.73 ± 2.5	-18.16 ± 1.0

The received power statistics are listed in Tables 6.8 and 6.9. The VV and VH experimental CDF's are plotted with the Weibull and Rayleigh CDF's in Figure 6.6. The VV and HH normalized power variances are small because the metal I-Beam backscatter is relatively uniform. The Rayleigh distribution is the best match for all polarizations. The VH CDF is not affected by the radar system MDS level.

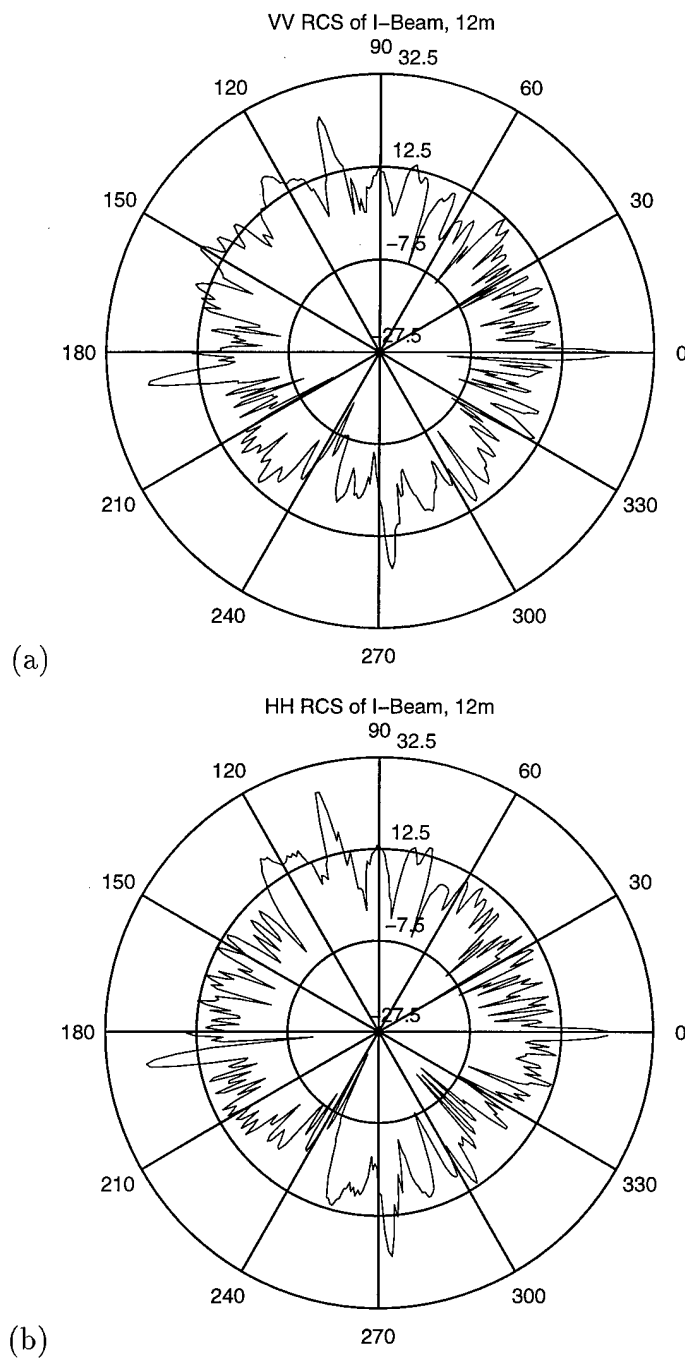


Figure 6.5: I-Beam RCS (dBsm) at 12m (a) VV Pol. (b) HH Pol.

Table 6.8: I-Beam Received Power Statistics, 12m

Pol.	Var.	\hat{b}	\hat{c}	x_{max}	χ^2 Weib.	χ^2 Ray.
VV	6.14	0.1091	0.3007	24.90	28.34	18.60
HH	8.66	0.1015	0.2959	32.88	28.67	20.16
VH	12.12	0.0961	0.2925	50.13	35.75	11.13

Table 6.9: I-Beam Received Power Statistics, 16m

Pol.	Var.	\hat{b}	\hat{c}	x_{max}	χ^2 Weib.	χ^2 Ray.
VV	5.59	0.1116	0.3023	21.0	32.30	6.35
HH	6.89	0.1063	0.2989	21.5	30.59	11.20
VH	11.91	0.0964	0.2926	38.0	34.70	13.31

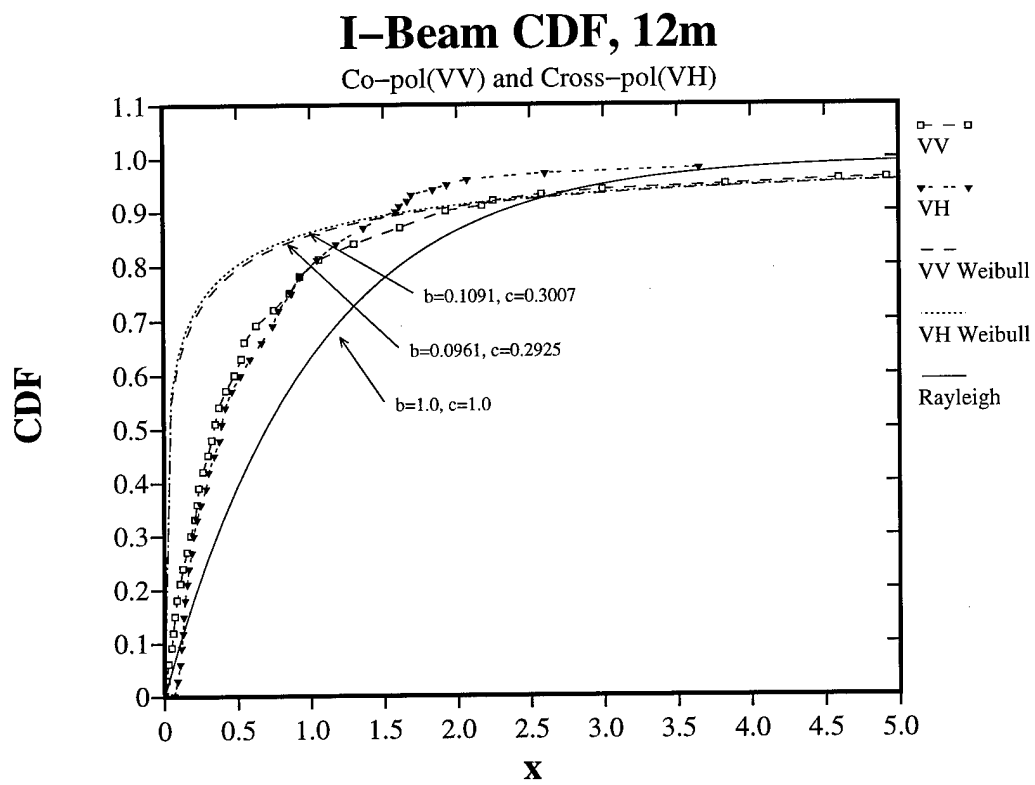


Figure 6.6: I-Beam CDF, 12m

6.4 Utility Post, Metal

A metal utility post is the next target presented. Utility posts are commonly used with temporary signs, such as construction zone signs. A utility post has an irregular shape, with dimensions 3.3 cm x 3.2 cm (1 5/16 in x 1 1/4 in). The top and front views of the post are shown in Figures C.7 and C.8, in Appendix C.

The utility post RCS, for σ_{VV} and σ_{HH} , are plotted in Figure 6.7(a) and (b). The non-uniform shape is clearly evident in the polar plots. The RCS is minimum along the back of the post. The σ_{VV} and σ_{HH} polar plots are noticeably different. These differences can be attributed to the irregular object shape. The average sigma values are listed in Table 6.10. Again, the $\langle \sigma_{VV} \rangle$ values are higher than $\langle \sigma_{HH} \rangle$ at 12 and 16 m. The VH average values are interesting, since the $\langle \sigma_{VH} \rangle$ value is larger at 16 m than at 12 m.

Table 6.10: Utility Post RCS Results

Pol.	$\langle \bar{\sigma} \rangle$ (dBsm), at 12m	$\langle \bar{\sigma} \rangle$ (dBsm), at 16m
VV	11.07 ± 0.9	5.25 ± 1.1
HH	7.57 ± 0.9	4.65 ± 1.0
VH	-24.15 ± 2.0	-20.51 ± 1.0

The received power statistics are listed in Tables 6.11 and 6.12. The experimental CDF's are plotted, along with the estimated Weibull and Rayleigh CDF in Figure 6.8. The VV and HH experimental CDF best match the Weibull distribution. The VV CDF tail, at $x \geq 2.5$, follows the Weibull distribution very closely. The VH experimental CDF matches the Rayleigh distribution very well. The VH measurements do not appear to be affected by the radar system MDS level. The received power statistics are similar at both 12 and 16 m.

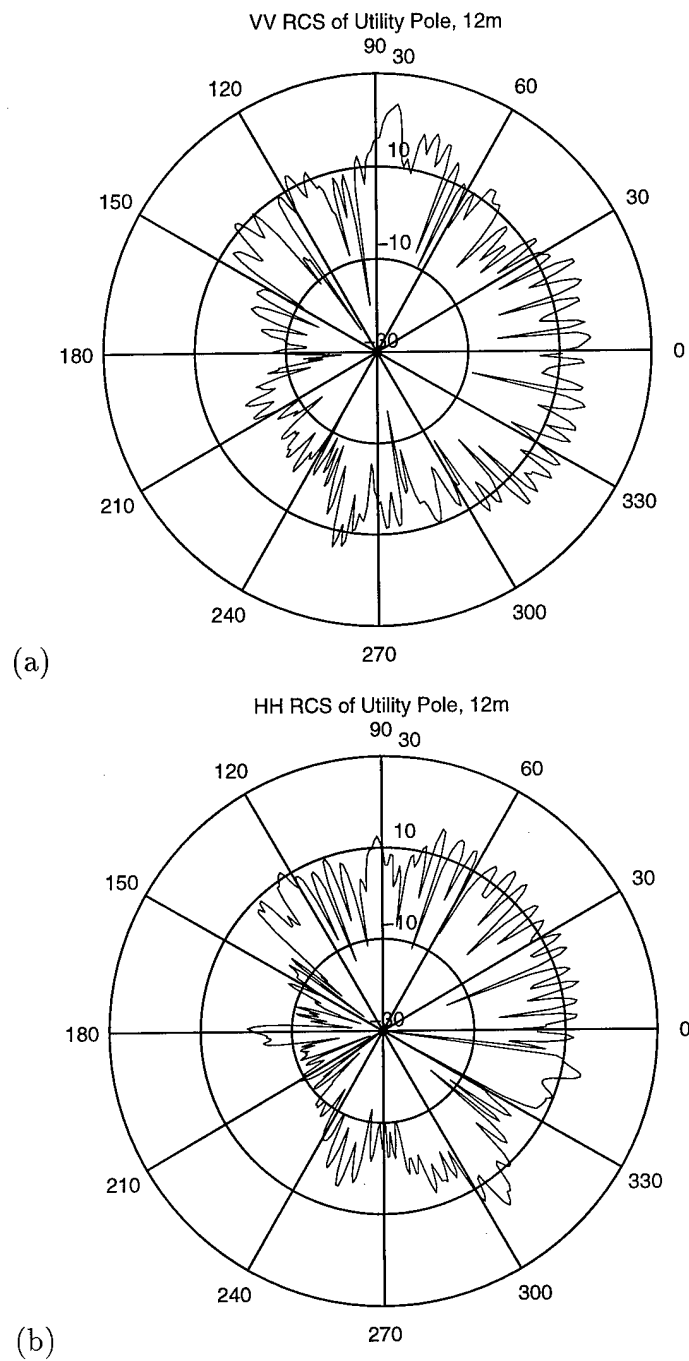


Figure 6.7: Utility Post RCS (dBsm) at 12m (a) VV Pol. (b) HH Pol.

Table 6.11: Utility Post Received Power Statistics, 12m

Pol.	Var.	\hat{b}	\hat{c}	x_{max}	χ^2 Weib.	χ^2 Ray.
VV	3.72	0.1256	0.3106	19.19	17.82	72.62
HH	2.25	0.1510	0.3249	9.63	12.91	123.4
VH	0.98	0.2183	0.3598	5.18	33.15	2.03

Table 6.12: Utility Post Received Power Statistics, 16m

Pol.	Var.	\hat{b}	\hat{c}	x_{max}	χ^2 Weib.	χ^2 Ray.
VV	3.42	0.1291	0.3126	18.66	16.84	88.40
HH	2.18	0.1531	0.3260	10.98	18.27	46.40
VH	1.14	0.2033	0.3527	7.37	34.03	2.22

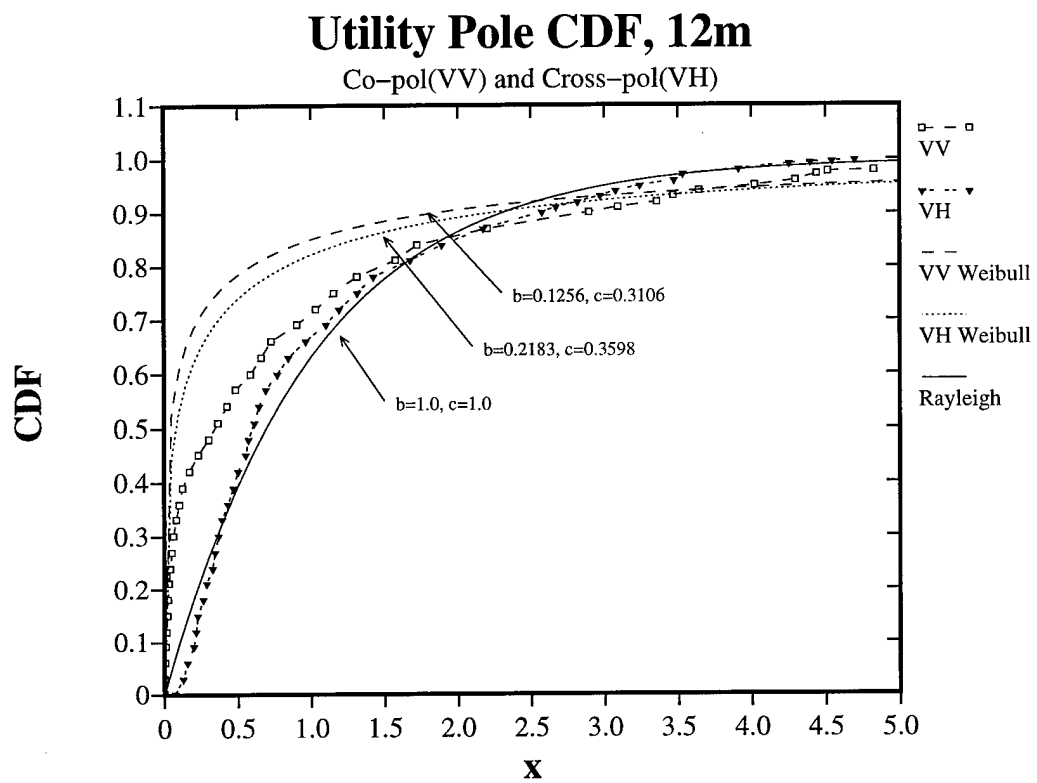


Figure 6.8: Utility Post CDF, 12m

6.5 Small U-Channel, Metal

The next target measured is a metal U-Channel post. Both a large and small U-Channel post were measured. The large U-Channel results are presented in the next section. The small U-Channel post commonly used with highway mile markers and highway reflectors. The post is U shaped, with dimensions 5.4 cm x 2.2 cm (2 1/8 in x 15/16 in). The top and front views of the U-Channel post are shown in Appendix C.

The U-Channel post RCS, for σ_{VV} and σ_{HH} , are plotted in Figure 6.9(a) and (b). The non-uniform object shape is clearly seen in the polar plots. The VV and HH RCS plots are different, especially from 120° to 240°. The HH RCS values are also larger along the backside of the object. The co-polarized scattering is greatly affected by shape irregularities.

The average sigma values were also computed, and are listed in Table 6.13. The $\langle\sigma_{VV}\rangle$ and $\langle\sigma_{HH}\rangle$ values are very similar. The measured HH average RCS is actually higher than the VV average at 16 m. The $\langle\sigma_{VH}\rangle$ value is again higher at 16 m than at 12 m.

Table 6.13: Small U-Channel RCS Results

Pol.	$\langle\bar{\sigma}\rangle$ (dBsm), at 12m	$\langle\bar{\sigma}\rangle$ (dBsm), at 16m
VV	10.11 ± 0.9	5.50 ± 0.8
HH	8.98 ± 0.7	6.54 ± 1.2
VH	-23.65 ± 2.5	-20.38 ± 1.3

The received power statistics are listed in Tables 6.14 and 6.15. The experimental CDF is plotted, along with the estimated Weibull and Rayleigh CDF in Figure 6.10. The normalized power variance is increased when increasing the target distance. This

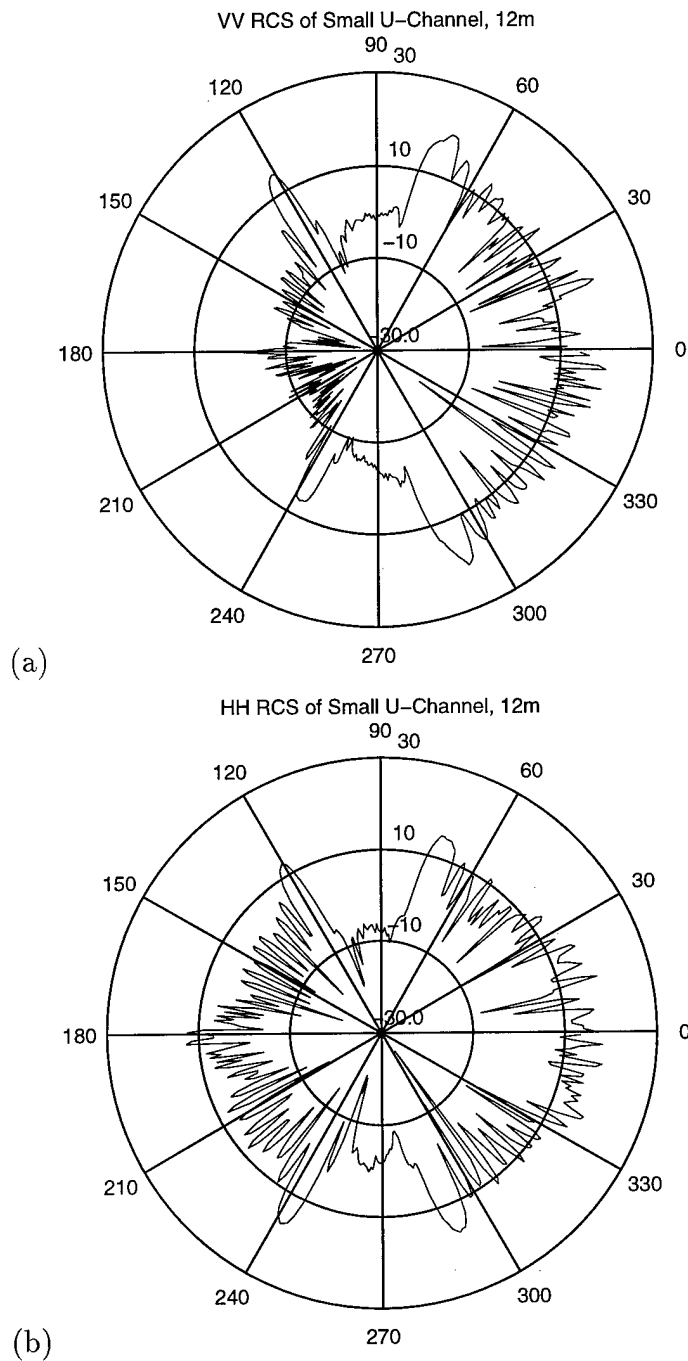


Figure 6.9: Small U-Channel RCS(dBsm) at 12m (a) VV Pol. (b) HH Pol.

affects both VV, HH and especially the VH experimental CDF. The VV and HH experimental CDF's best match the Weibull distribution at both distances. The VH CDF matches best matches the Weibull distribution at 12 m and the Rayleigh distribution at 16 m.

Table 6.14: Small U-Channel Received Power Statistics, 12m

Pol.	Var.	\hat{b}	\hat{c}	x_{max}	χ^2 Weib.	χ^2 Ray.
VV	3.67	0.1261	0.3109	12.19	8.52	334.0
HH	2.39	0.1472	0.3228	9.08	18.89	48.31
VH	4.29	0.1201	0.3073	15.69	28.89	42.0

Table 6.15: Small U-Channel Received Power Statistics, 16m

Pol.	Var.	\hat{b}	\hat{c}	x_{max}	χ^2 Weib.	χ^2 Ray.
VV	4.62	0.1175	0.3058	14.71	9.43	663.49
HH	4.23	0.1206	0.3076	13.32	5.35	1093.1
VH	2.56	0.1433	0.3207	10.33	33.22	9.95

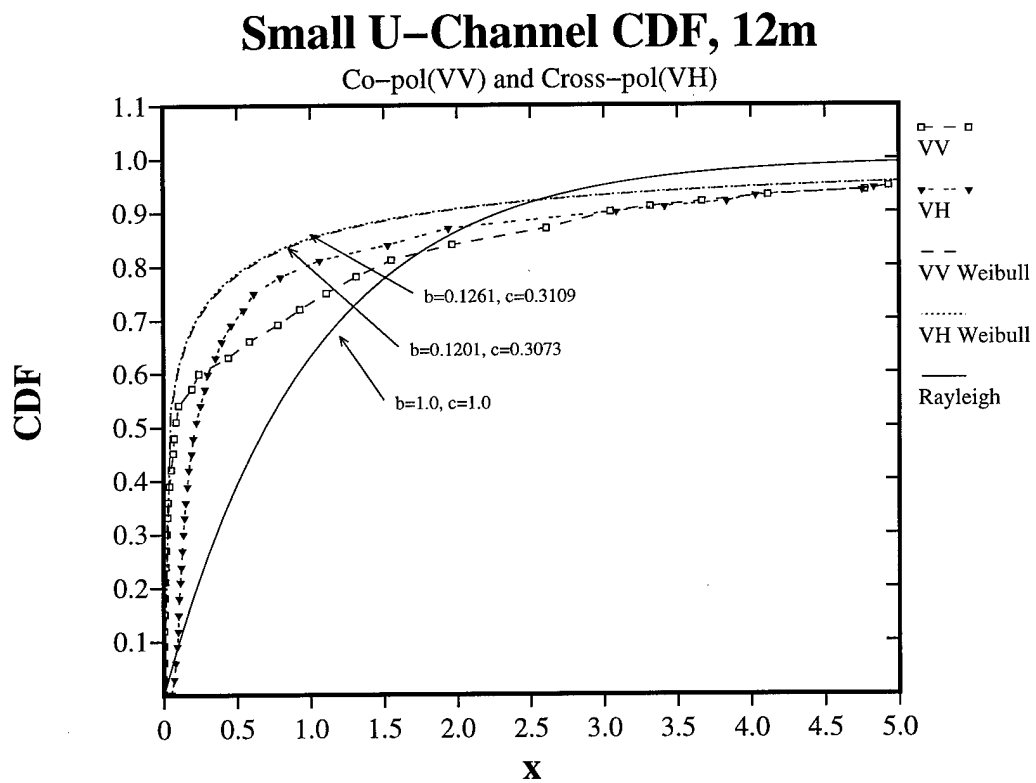


Figure 6.10: Small U-Channel CDF, 12m

6.6 Large U-Channel, Metal

The sixth target measured is a large U-Channel post. The large U-Channel post is the most common sign post. It is used several signs, including stop signs and no parking signs. The post is U shaped, with dimensions 7.85 cm x 3.7 cm (3 1/8 in x 1 1/2 in). Figures C.11 and C.12, in Appendix C, show both the top and front views.

The large U-Channel RCS, for σ_{VV} and σ_{HH} , are plotted in Figure 6.11(a) and (b). The non-uniform object shape is again evident in the polar plots. The VV and HH RCS results are similar, contrary to the small U-Channel measurements. The VV average sigma value is higher than the HH average. The average sigma values are listed in Table 6.16. The $\langle \overline{\sigma_{VH}} \rangle$ is larger at 16 m than at 12 m.

Table 6.16: Large U-Channel RCS Results

Pol.	$\langle \overline{\sigma} \rangle$ (dBsm), at 12m	$\langle \overline{\sigma} \rangle$ (dBsm), at 16m
VV	13.6 ± 0.7	10.44 ± 1.0
HH	10.38 ± 0.9	8.40 ± 0.9
VH	-21.33 ± 3.0	-18.83 ± 1.0

The received power statistics are listed in Tables 6.17 and 6.18. The experimental CDF's are plotted, along with the estimated Weibull and Rayleigh CDF in Figure 6.12. The experimental CDF results, for all polarizations, are effected when increasing the target distance. An increase in the normalized power variance is the result. The VV and HH experimental CDF plots still best match the Weibull distribution at both distances. The VH experimental CDF best matches the Weibull distribution at 12 m. The VV and VH tail distribution, for $x \geq 2.5$, matches the Weibull distribution very closely. At 16 m, the VH CDF matches the Rayleigh and Weibull distribution equally well.

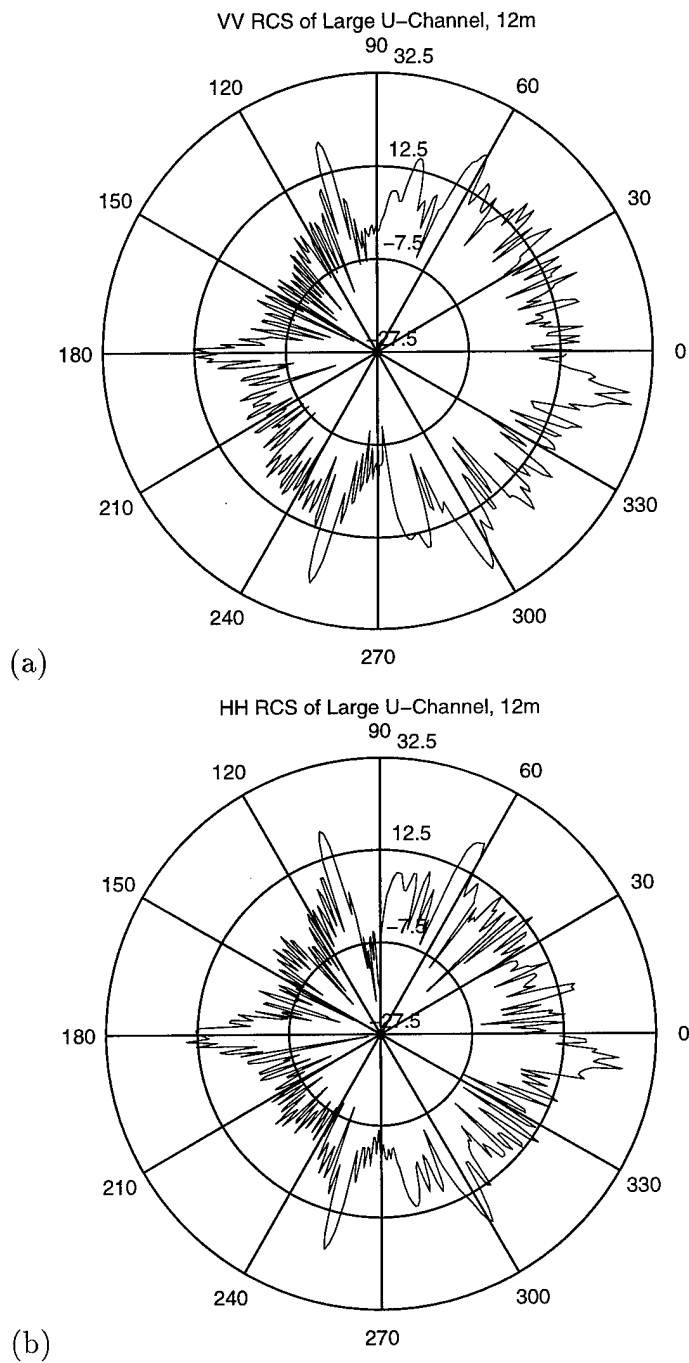


Figure 6.11: Large U-Channel RCS(dBsm) at 12m (a) VV Pol. (b) HH Pol.

Table 6.17: Large U-Channel Received Power Statistics, 12m

Pol.	Var.	\hat{b}	\hat{c}	x_{max}	χ^2 Weib.	χ^2 Ray.
VV	7.65	0.1041	0.2975	34.20	16.85	128.4
HH	8.31	0.1023	0.2964	37.43	19.07	97.12
VH	7.86	0.1034	0.2971	32.42	25.30	84.30

Table 6.18: Large U-Channel Received Power Statistics, 16m

Pol.	Var.	\hat{b}	\hat{c}	x_{max}	χ^2 Weib.	χ^2 Ray.
VV	13.48	0.0948	0.2916	37.55	12.02	279.8
HH	17.39	0.0920	0.2898	48.95	9.98	415.7
VH	8.18	0.1026	0.2966	29.40	32.63	34.56

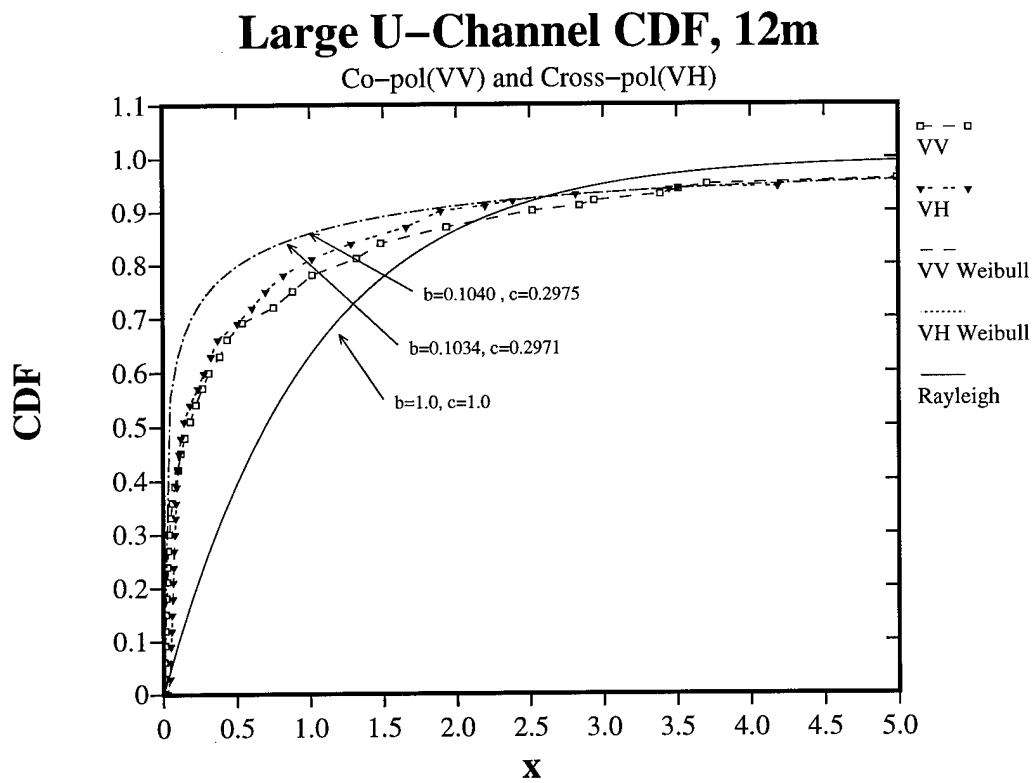


Figure 6.12: Large U-Channel CDF, 12m

6.7 Guard Rail Measurements

A section of Guard Rail is the last target presented. The Guard Rail is rectangular shaped, with dimensions 32.4 cm x 8.36 cm (12 3/4 in x 3 1/4 in). The Guard Rail section top and front are shown in Figures C.13 and C.14, in Appendix C.

The Guard Rail measurements were performed at 15 and 20 m. An increase in distance was necessary because receiver saturation occurred at 12 m. The Guard Rail RCS, σ_{VV} and σ_{HH} , are plotted in Figure 6.13(a) and (b). The VV and HH σ plots are very similar. The minimum RCS values occur at the Guard Rail edges, at approximately 90° and 270° . The average sigma values are similar for both VV and HH polarizations. The average sigma values are listed in Table 6.19. The VH average RCS values differ significantly when increasing the target distance to 20 m.

Table 6.19: Guard Rail RCS Results

Pol.	$\langle \bar{\sigma} \rangle$ (dBsm), at 15m	$\langle \bar{\sigma} \rangle$ (dBsm), at 20m
VV	17.96 ± 1.0	16.77 ± 0.9
HH	16.43 ± 1.3	15.86 ± 1.5
VH	-6.97 ± 3.9	-10.83 ± 4.5

The received power statistics are listed in Tables 6.20 and 6.21. The experimental CDF is plotted, along with the estimated Weibull and Rayleigh CDF in Figure 6.14. The Guard Rail shape is fairly uniform, causing the normalized power variance to be small. The VV and HH experimental CDF's match the Weibull and Rayleigh distributions equally well at 15 m. At 20 m, the VV and HH CDF's better match the Rayleigh distribution. The VH experimental CDF best matches the Rayleigh distribution at both 15 and 20 m. The VH polarization measurements appear to be above the radar system noise level.

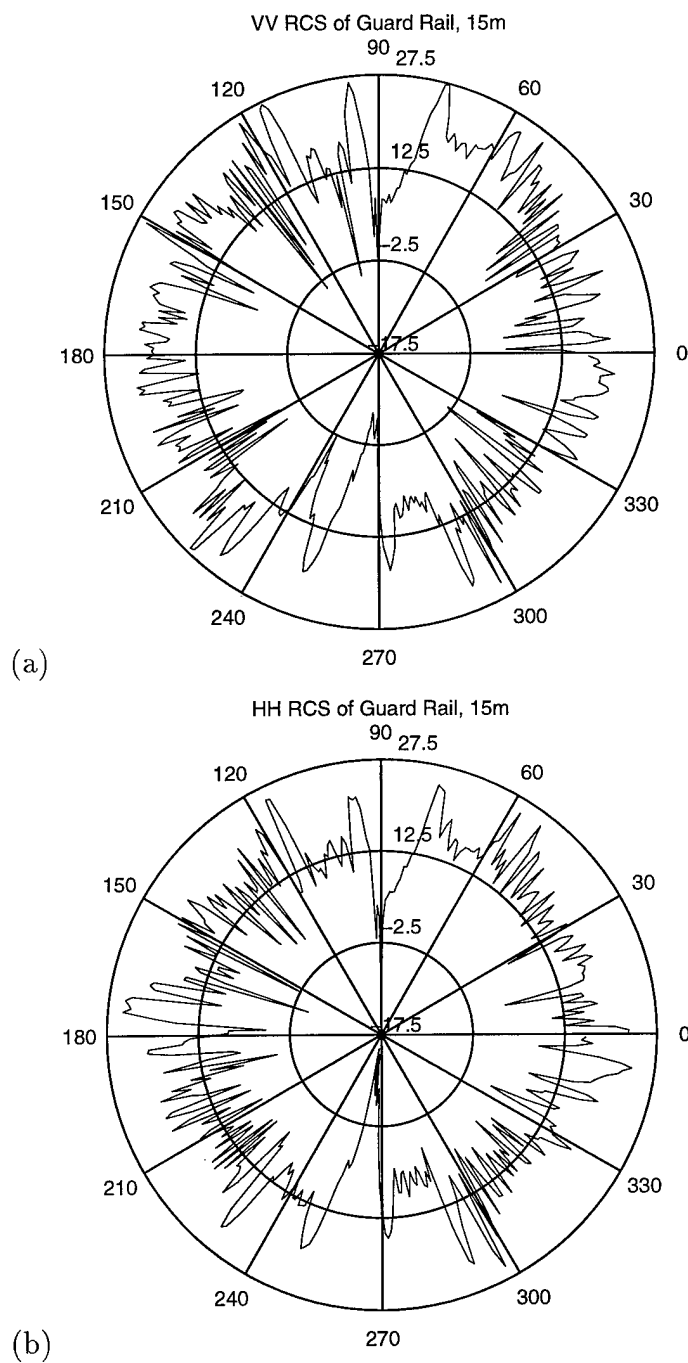


Figure 6.13: Guard Rail RCS(dBsm) at 15m (a) VV Pol. (b) HH Pol.

Table 6.20: Guard Rail Received Power Statistics, 15m

Pol.	Var.	\hat{b}	\hat{c}	x_{max}	χ^2 Weib.	χ^2 Ray.
VV	3.21	0.1320	0.3142	15.21	28.19	20.21
HH	2.94	0.1362	0.3166	14.86	22.74	24.88
VH	3.43	0.1289	0.3125	17.18	28.62	8.41

Table 6.21: Guard Rail Received Power Statistics, 20m

Pol.	Var.	\hat{b}	\hat{c}	x_{max}	χ^2 Weib.	χ^2 Ray.
VV	3.43	0.1290	0.3125	17.64	24.68	17.18
HH	3.08	0.1338	0.3153	13.86	26.69	10.68
VH	3.45	0.1287	0.3124	18.77	31.10	9.65

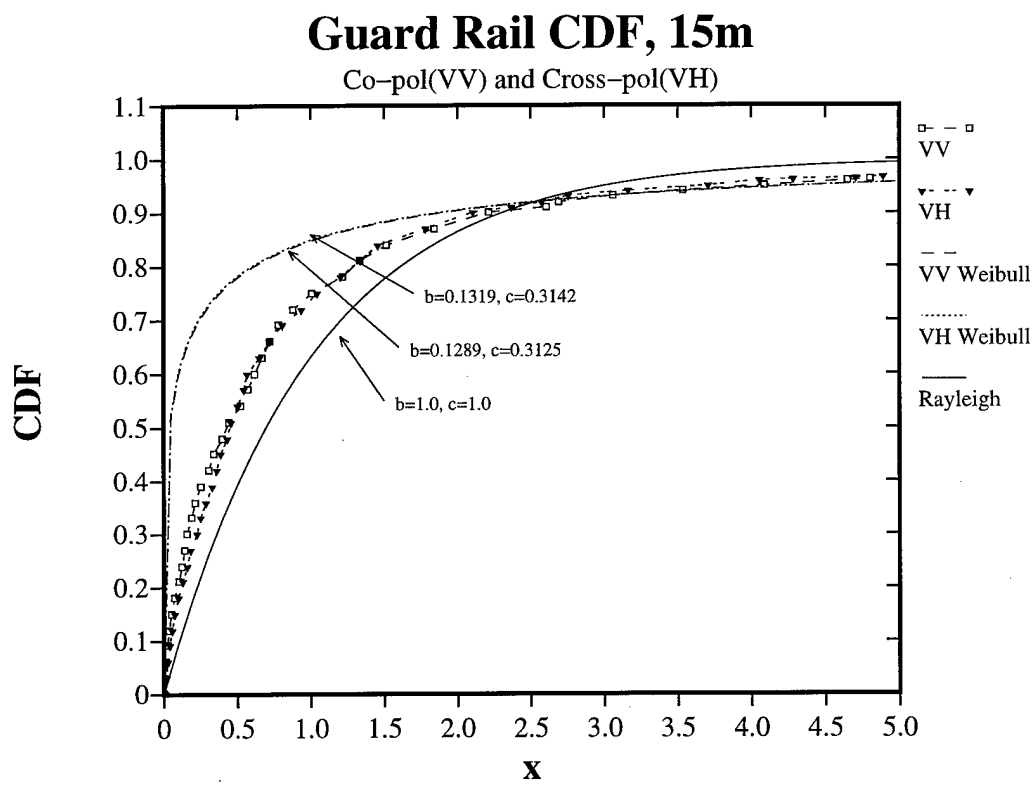


Figure 6.14: Guard Rail CDF, 15m

Chapter 7

Conclusions

This thesis documents and analyzes measured grazing angle surface clutter and roadside object radar cross-sections obtained using a 95 GHz radar system. A super heterodyne receiver down-converts the received 95 GHz signal, in two stages, to 60 MHz. A 60 MHz logarithmic amplifier detector converts the received signal power to a corresponding voltage. The logarithmic amplifier dynamic range is -80 to 0 dBm. The radar system output voltage was sampled and stored by a PC controlled A/D board. Each sampled voltage was then interpolated from the logarithmic amplifier calibration curve, to provide received power levels.

The radar system minimum detectable signal (MDS) level and the transmitted power limited the grazing angle clutter measurements. The cross-pol received power was lower than the system noise level at grazing angles less than 5.0° . A minimum target distance of 10.2 m is set by the far-field distance restriction. This requirement limits the largest attainable grazing angle to approximately 8.8° . The radar system transmitted power is 40 mW. The overall receiver noise figure is 12.3 dB, resulting in a MDS level of approximately -54.0 dBm. The radar system could be improved by increasing the transmitted signal power or reducing the receiver noise figure. Adding a

95 GHz TWT amplifier to the Gunn Oscillator source would increase the transmitted power by 30 to 40 dB. Grazing angle measurements at less than 5.0° would then be possible.

Grazing angle surface clutter, at 7.5° and 5.0° , was measured for asphalt, dry snow, dry soil, gravel and grass surfaces. Average normalized RCS values and the normalized received power statistics were analyzed. All surfaces at 7.5° and 5.0° were considered "rough" based upon the Rayleigh roughness criterion. The average sigma-zero values, for all polarizations, decreased when varying the grazing angle from 7.5° to 5.0° . This thesis presents the first known low grazing angle clutter results for grass, bare soil and gravel surfaces.

The Georgia Tech snow clutter model exists only for new snow and refrozen snow surfaces. The dry snow experimental sigma-zero values thus could not be compared directly to the Georgia Tech model. The clutter model does underestimate the change in sigma-zero, when changing the angle from 7.5° to 5.0° grazing. The clutter model suggests a 2 to 3 dB change, but our experimental results show an 8 to 10 dB difference in the average sigma-zero values. The asphalt experimental results were compared to previously published values. Our results were 4 dB larger at 7.5° grazing, and 3 to 4 dB smaller at a 5.0° grazing angle.

The normalized received power statistics were compared to Weibull and Rayleigh probability distributions. For all surface types, the surface roughness is uniformly distributed, with no dominant scattering centers. Therefore, the normalized power statistics best matched the Rayleigh assumption. The MDS level effect, especially for VH polarization measurements at 5.0° grazing, were noticeable on the normalized power CDF plots. The average sigma-zero values are overestimated when the MDS level affects the received signal. The asphalt surface was the smoothest surface, and

was thus affected most by the radar system noise level due to the lower received power.

The variability between wet and dry gravel is approximately 6 to 10 dB, for all polarizations. For the grass surfaces, the co-polarized values varied by 2 to 3 dB, because of the grass height variance. The cross-pol grass measurements varied less, because the diffuse scattering depends on the underlying surface. More effort is needed to characterize sigma-zero variability, resulting from changes in environmental conditions. Surface clutter measurements of other surface types would also be beneficial. Data from new and refrozen snow types could be compared directly to the Georgia Tech clutter model.

Radar cross-section measurements were obtained for several common roadside objects. Six different sign posts and a section of guard rail were measured. An azimuthal RCS profile is plotted for each object, at both VV and HH polarizations. The RCS measurements are important for automobile collision avoidance radar systems. The received power statistics are particularly important when designing a constant false alarm rate (CFAR) radar system. The roadside object normalized power measurements are compared to both the Rayleigh and Weibull probability distributions. This thesis presents the first 95 GHz RCS measurements of common sign-posts and a guard rail section.

The object RCS, or sigma values, were plotted as a function of azimuth angle. The HH and VV values are presented in a polar plot. The VV sigma values are higher than the HH values, because of the vertical target orientation. The sign-posts and guard rail are assumed to be point targets when computing a RCS value at each sample point. However, the object area illuminated is affected when changing the target distance. An overall average RCS value was thus computed at two target distances, in order to determine the effect of a larger illuminated target area. The

average sigma values decreased by 2 to 3 dB when increasing the target distance. Unsuccessful approximations were made, but not discussed in this thesis, to explain this change in average RCS. A normalized ratio of illuminated target area to the total beam area was computed, but did not successfully explain the change in average RCS values. Computation of the average illuminated target area is difficult for irregular shaped objects. Further analysis is needed to characterize the change in RCS with distance.

The normalized power statistics were considered at both target distances. Changing the target distance had little effect on the normalized power statistics. This suggests that the normalized power results hold at any target distance. The uniform shaped targets, i.e. the round wood pole and guard rail section, best match the Rayleigh probability assumption. The RCS of a larger object has a smaller variance. The scattering from smaller, irregular shaped objects, such as the U-Channel, square wood pole and utility post, best matched the Weibull probability distribution. The irregular shaped objects had a much higher normalized power variance.

Several other roadside objects could be measured. Light posts, reflective barricades and fire hydrants are just a few examples. Automobile RCS measurements are also important for collision avoidance systems.

Appendix A

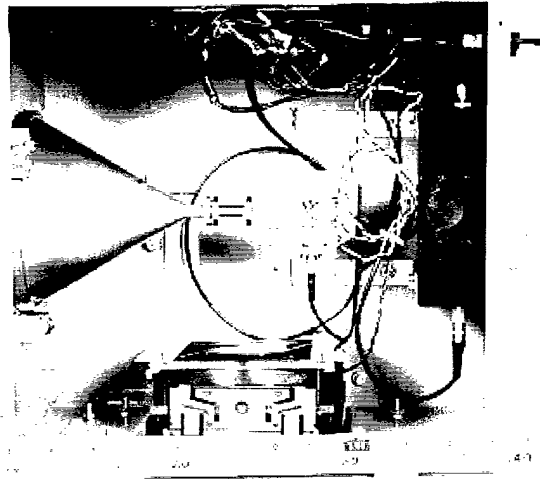


Figure A.1: MMW Radar Transmitter

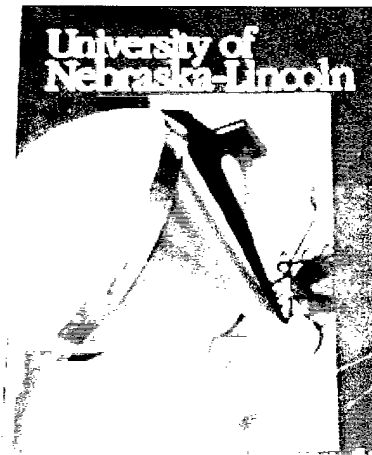


Figure A.2: Dielectric Horn Antenna

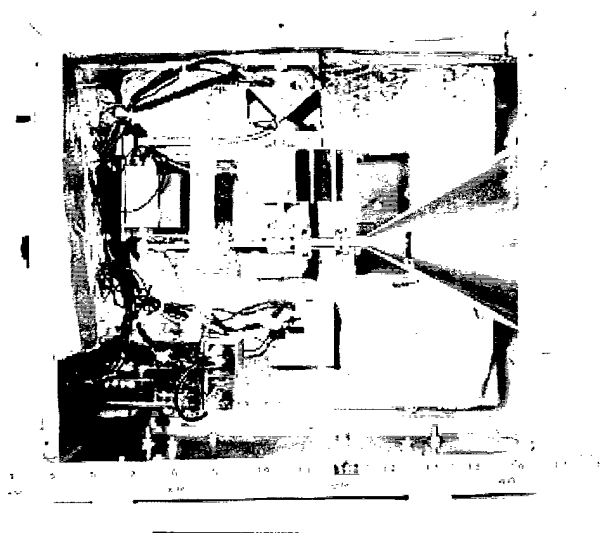


Figure A.3: MMW Radar Receiver



Figure A.4: HP-8620C Sweep Oscillator

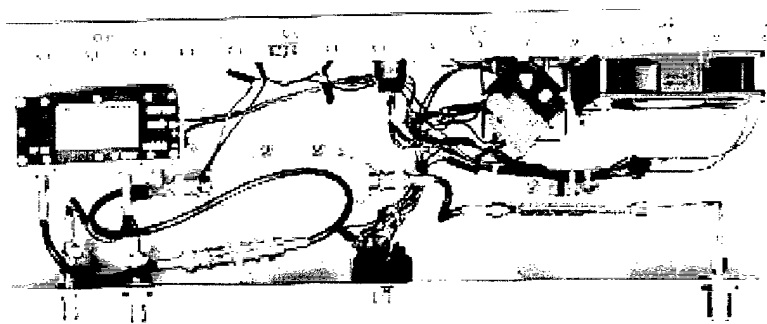


Figure A.5: 2nd IF Stage

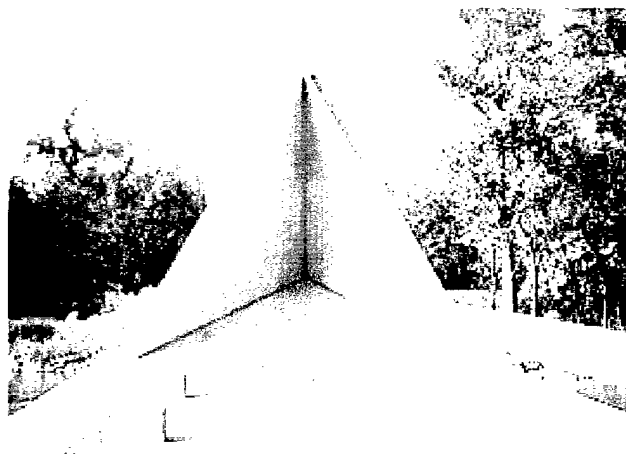


Figure A.6: Tetrahedral Corner Reflector

Appendix B

Table B.1: Asphalt Surface Ground Truth

Condition	Δh	Rough Criteria
Dry	1.5 cm	$\Theta_g \geq 1.51^\circ$

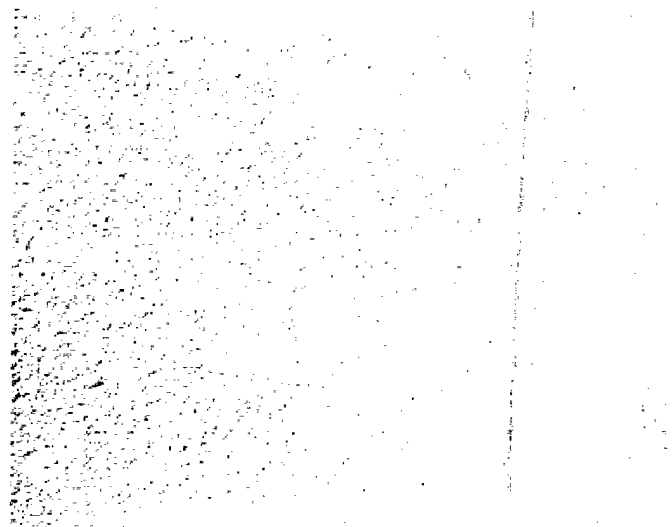


Figure B.1: Asphalt Surface

Table B.2: Gravel Surface Ground Truth

Condition	Avg. Depth	Gravel Size	Δh	Rough Criteria
Wet and Dry	10.15 cm	2 to 5 cm	4.0 cm	$\Theta_g \geq 0.57^\circ$



Figure B.2: Dry Gravel Surface

Table B.3: Dry Snow Ground Truth

Condition	Avg. Depth	Δh	Rough Criteria
Dry	9.4 cm	3.0 cm	$\Theta_g \geq 0.75^\circ$

Figure B.3: Dry Snow Surface

Table B.4: Dry Soil Ground Truth

Condition	Δh	Rough Criteria
Dry, Bare	7.5 cm	$\Theta_g \geq 0.30^\circ$

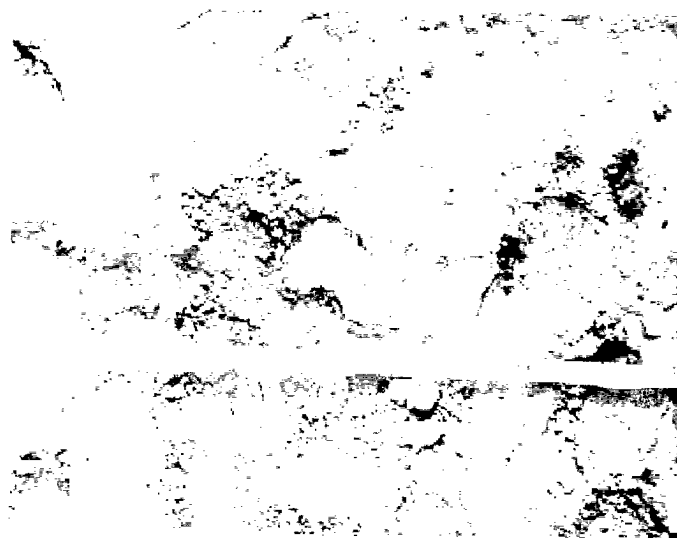


Figure B.4: Dry Soil Surface

Table B.5: Short Grass Ground Truth

Condition	Avg. Height	Δh	Rough Criteria
Dormant, Dry	3.5 cm	4.0 cm	$\Theta_g \geq 0.57^\circ$

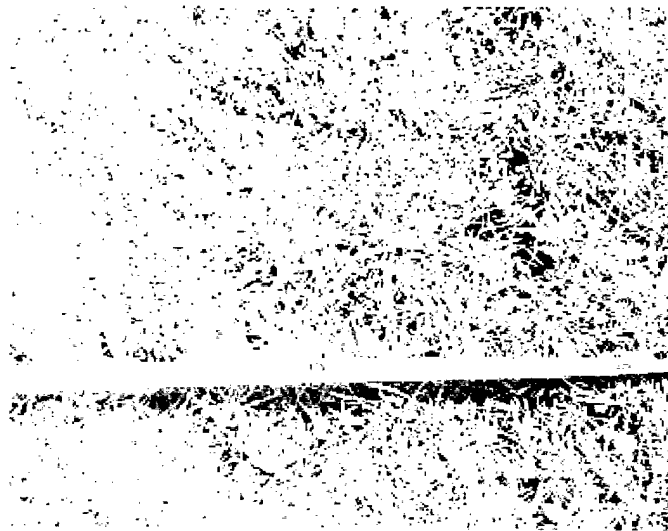


Figure B.5: Short Grass Surface

Table B.6: Tall Grass Ground Truth

Condition	Avg. Height	Δh	Rough Criteria
Dormant, Dry	9.0 cm	7.0 cm	$\Theta_g \geq 0.32^\circ$

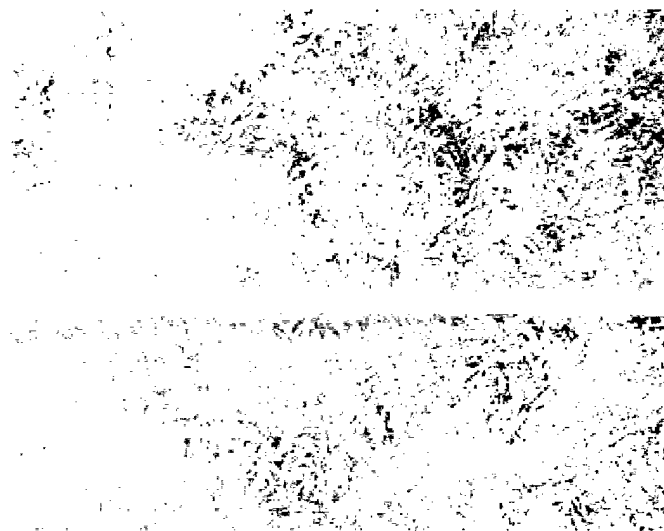


Figure B.6: Tall Grass Surface

Appendix C

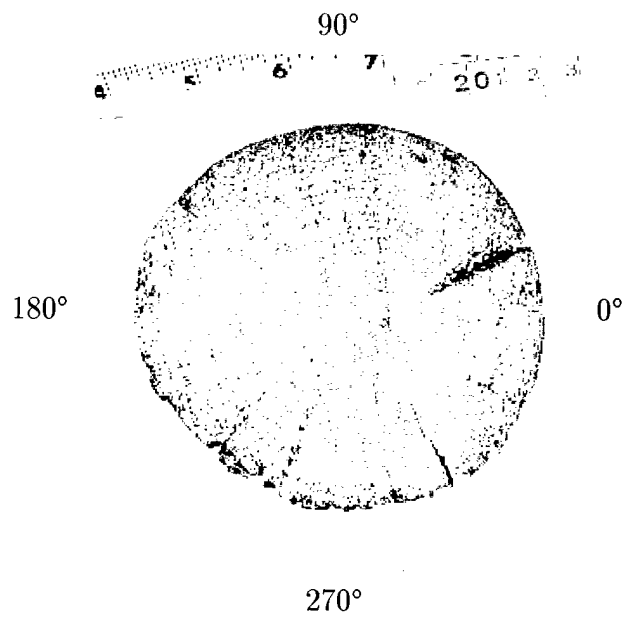


Figure C.1: Top, Round Wood Pole

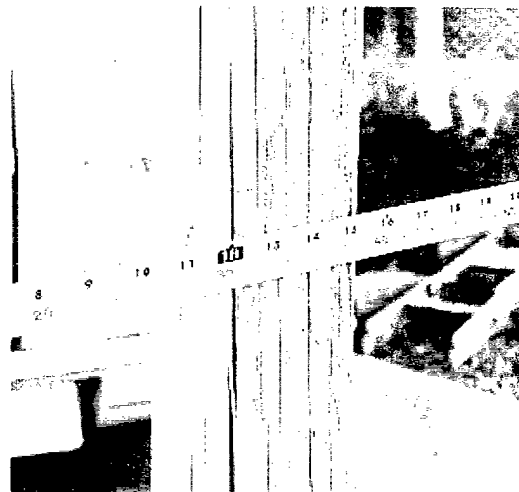


Figure C.2: Round Wood Pole

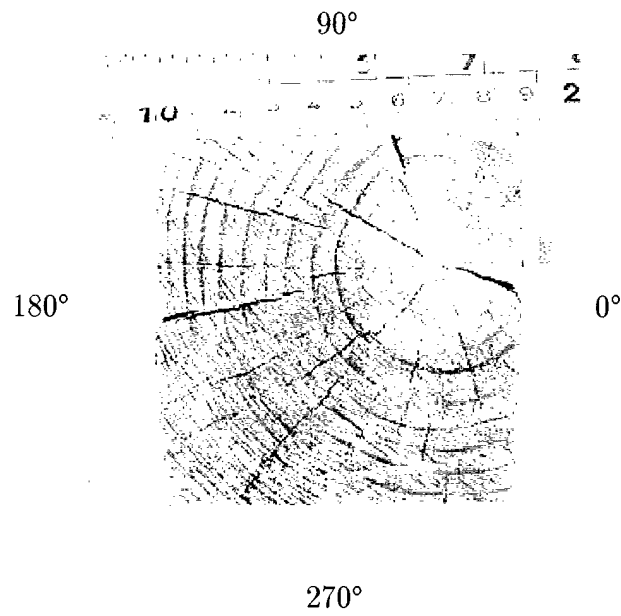


Figure C.3: Top, Square Wood Pole

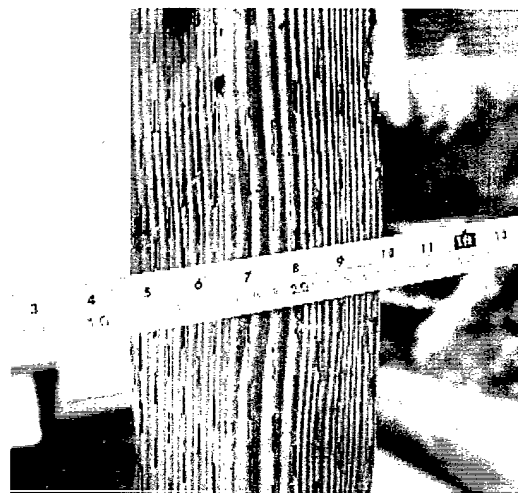


Figure C.4: Square Wood Pole

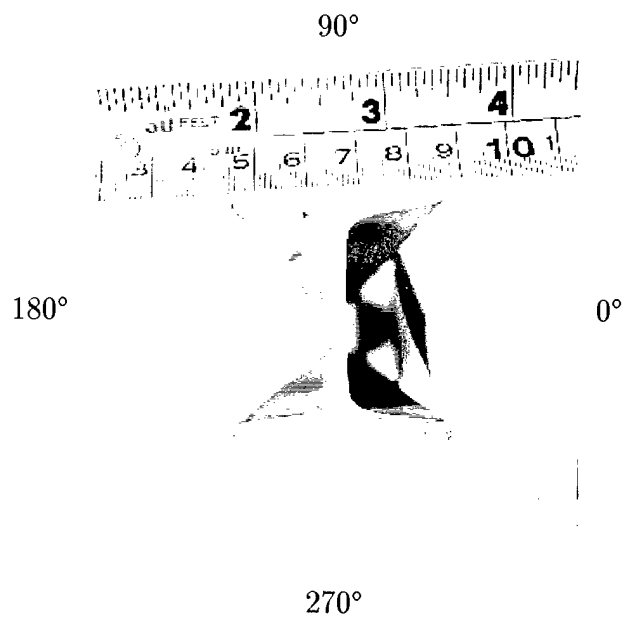


Figure C.5: Top, I-Beam Post



Figure C.6: I-Beam Post

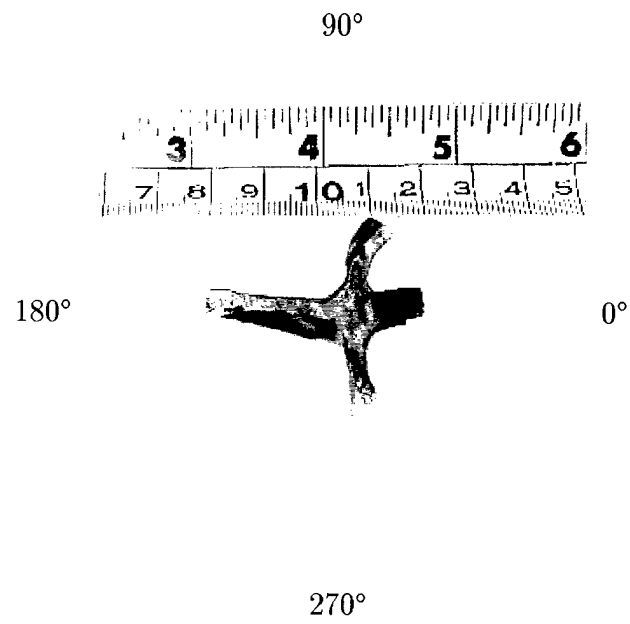


Figure C.7: Top, Utility Post

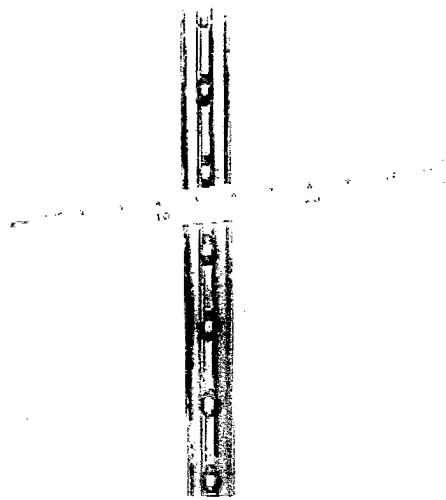


Figure C.8: Utility Post

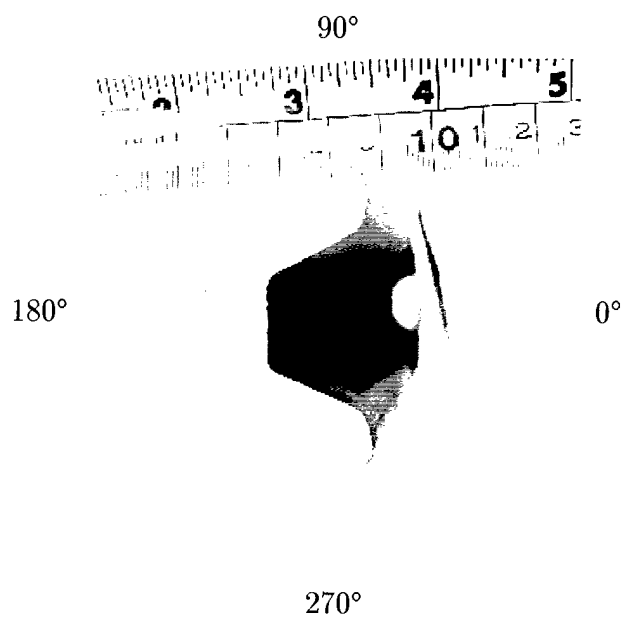


Figure C.9: Top, Small U-Channel Post

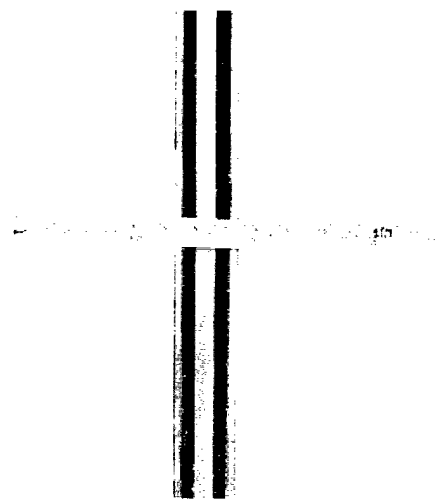


Figure C.10: Small U-Channel Post

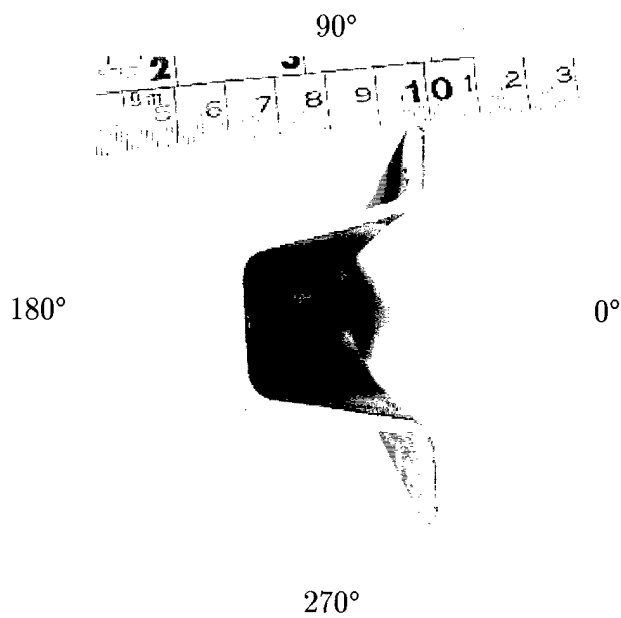


Figure C.11: Top, Large U-Channel Post

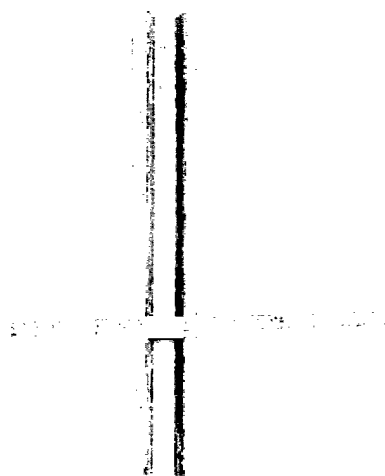


Figure C.12: Large U-Channel Post

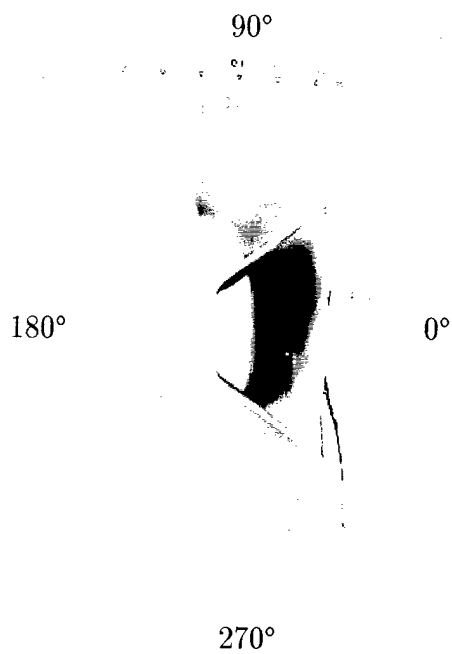


Figure C.13: Top, Guard Rail Section

Figure C.14: Guard Rail Section

Bibliography

- [1] B.W. Henderson, New MMIC Chips Could Make Millimeter-Wave Radar Affordable, *Aviation Week and Space Technology*, March 26, 1990, v132, n13, pp. 78-79.
- [2] B.D. Nordwall, Millimeter-Wave Radar Tested as a Landing Aide, *Aviation Week and Space Technology*, May 15, 1995, v142, n20, pp. 55-56.
- [3] N.C. Currie, R.D. Hayes and R.N. Trebits, *Millimeter-Wave Radar Clutter*, Artech House, 1992, pp. 19-23, 147-150.
- [4] H. Yamaguchi et al., A Study on 94 GHz Millimeter-Wave RCS Characteristics, *Proceedings of the 1996 IEEE National Radar Conference*, IEEE Press, 1996, pp. 333-338.
- [5] M.W. Long, *Radar Reflectivity of Land and Sea*, 2nd Ed., Artech House, 1983, pp. 36-39.
- [6] P.L. Lowbridge, Low Cost Millimeter-Wave Radar Systems for Intelligent Vehicle Cruise Control Applications, *Microwave Journal*, October 1995, v38, n10, pp. 20-28.
- [7] L. Rafaelli and E. Stewart, Millimeter-Wave Monolithic Components for Automotive Applications, *Microwave Journal*, February 1992, v35, n2, pp. 22-32.

- [8] L.H. Eriksson and B.O. As, A High Performance Automotive Radar for Automatic AICC, *IEEE AES Systems Magazine*, December 1995, v10, n12, pp. 13-17.
- [9] M.I. Skolnik, *Radar Handbook*, 2nd Ed., McGraw-Hill, 1990, pp. 2.4-2.6.
- [10] M.I. Skolnik, *Introduction to Radar Systems*, 2nd Ed., McGraw-Hill, 1980, pp. 23, 344-346.
- [11] N.C. Currie and C.E. Brown, *Principles and Applications of Millimeter-Wave Radar*, Artech House, 1987, pp. 602-603.
- [12] W. C. Morchin, *Radar Engineer's Sourcebook*, Artech House, 1993, pp. 95-96.
- [13] F.T. Ulaby, R.D. Moore and A.K. Fung, *Microwave Remote Sensing, Volume II*, Addison-Wesley, 1982, pp. 585-586.
- [14] R.E. Walpole and R.H. Meyers, *Probability and Statistics for Engineers and Scientists*, 5th Ed., Macmillan Publishing, 1989, pp. 344-346.
- [15] W.H. Beyer, *CRC Handbook of Tables for Probability and Statistics*, 2nd Ed., Chemical Rubber Company, 1968, pp. 293-295.
- [16] S.D. Robertson, *Bell System Technical Journal*, vol. 26, 1947, pp. 852-854.
- [17] R.S. Burington and D.C. May Jr., *Handbook of Probability and Statistics with Tables*, 2nd Ed., McGraw-Hill, 1970, pp. 90-91.
- [18] R.M. Narayanan, *Measurement and Analysis of Electromagnetic Scattering from Vegetation and Fallen Snow at 215 GHz*, PhD. Dissertation, Univ. of Massachusetts-Amherst, Sept. 1988, pp. 38-42.